The Astrophysical Journal, 625:307–323, 2005 May 20

ULTRAVIOLET, X-RAY, AND OPTICAL RADIATION FROM THE GEMINGA PULSAR[1]

O. Y. Kargaltsev,[2] G. G. Pavlov,[2] V. E. Zavlin,[3] and R. W. Romani[4]

Received 2004 December 22; accepted 2005 February 2

ABSTRACT

We observed the γ-ray pulsar Geminga with the FUV-MAMA and NUV-MAMA detectors of the Space Telescope Imaging Spectrometer to measure Geminga's spectrum and pulsations in the ultraviolet. The slope of the far-ultraviolet (FUV) spectrum is close to that of a Rayleigh-Jeans spectrum, suggesting that the FUV radiation is dominated by thermal emission from the neutron star (NS) surface. The measured FUV flux, $F_{\rm FUV} = (3.7 \pm 0.2) \times 10^{-15}$ ergs cm^{-2} s^{-1} in the 1155–1702 Å band, corresponds to a brightness temperature $T_{\rm RJ} \approx (0.3–0.4)(d_{200}/R_{13})^2$ MK, depending on the interstellar extinction ($d = 200\,d_{200}$ pc and $R = 13R_{13}$ km are the distance and the NS radius, respectively). The soft thermal component of Geminga's X-ray spectrum measured with the *XMM-Newton* observatory corresponds to a temperature $T_s = 0.49 \pm 0.01$ MK and radius $R_s = (12.9 \pm 1.0)\,d_{200}$ km. Contrary to other NSs detected in the UV-optical, for which the extrapolation of the X-ray thermal component into the optical underpredicts the observed flux of thermal radiation, the FUV spectrum of Geminga lies slightly below the extrapolation of the soft thermal component, which might be associated with Geminga's very low temperature. Surprisingly, the thermal FUV radiation is strongly pulsed, showing a narrow dip at a phase close to that of a broader minimum of the soft X-ray light curve. The strong pulsations might be attributed to partial occultations of the thermal UV radiation by regions of the magnetosphere filled with electron/positron plasma. In contrast to the FUV spectrum, the near-infrared (NIR) through near-ultraviolet (NUV) spectrum of Geminga is clearly nonthermal. It can be described by a power-law model, $F_\nu \propto \nu^{-\Gamma+1}$, with a photon index $\Gamma = 1.43 \pm 0.15$, close to the slope $\Gamma = 1.56 \pm 0.24$ of the hard X-ray ($E > 2.5$ keV) magnetospheric component. The extrapolation of the X-ray magnetospheric spectrum into the optical is marginally consistent with (or perhaps lies slightly above) the observed NIR-optical-NUV spectrum. The NUV pulsations, however, do not show a clear correlation with the hard X-ray pulsations.

Subject headings: pulsars: individual (Geminga) — stars: neutron — ultraviolet: stars

1. INTRODUCTION

Spin-powered pulsars show highly pulsed emission from the radio to γ-rays, arising from acceleration zones in their magnetospheres. In the UV to soft X-ray band, however, thermal emission from the neutron star (NS) surface can contribute significantly for middle-aged pulsars, with characteristic ages $\tau \sim 10^4$–10^6 yr. Spectral and timing measurements can separate these two components, allowing a measure of the surface temperature and thermal luminosity. By measuring thermal emission as a function of age, one can probe the equation of state of matter at supranuclear densities in the NS core and constrain the surface composition. Observations with the *Chandra* and *XMM-Newton* X-ray observatories have begun to reveal much about the thermal component (see Pavlov et al. [2002] and Kaspi et al. [2006] for recent reviews). However, since typical effective temperatures of middle-aged pulsars are as low as ~30–100 eV, and interstellar absorption severely attenuates the flux below ~0.1 keV, the X-ray observations of these objects can only probe the Wien tail of the surface thermal spectrum. Two issues then complicate the interpretation. First, surface composition can dramatically affect the X-ray flux (Romani 1987; Zavlin & Pavlov 2002) with light element atmosphere leading to a large Wien excess. Second, any surface temperature inhomogeneities will also complicate the spectrum, with hot spots disproportionately important in the high-energy (X-ray) tail. For these reasons, comparison of the X-ray results with UV emission from the Rayleigh-Jeans side of the thermal bump is particularly valuable. The challenge here is that nonthermal magnetospheric emission becomes increasingly dominant as one moves to the red (Pavlov et al. 2002). Fortunately, the NUV-MAMA and FUV-MAMA detectors of the Space Telescope Imaging Spectrometer (STIS) aboard the *Hubble Space Telescope* (*HST*) offer access to the UV emission and provide the phase-resolved measurements that can help to separate the thermal and nonthermal fluxes.

We report here on *HST* STIS observations of the middle-aged γ-ray pulsar Geminga. Discovered in 1972 by the *SAS 2* satellite (Thompson et al. 1977), this object had been known only as a γ-ray source until it was detected in X-rays by the *Einstein* observatory (Bignami et al. 1983) and associated with a faint ($V \approx 25.5$) optical counterpart (Bignami et al. 1987; Bignami et al. 1988; Halpern & Tytler 1988). The discovery of a period $P = 237$ ms in X-rays with *ROSAT* (Halpern & Holt 1992) and in γ-rays with the *Compton Gamma Ray Observatory* (*CGRO*) (Bertch et al. 1992) proved the source to be a spin-powered pulsar, with a characteristic age $\tau \equiv P/(2\dot{P}) = 342$ kyr and spin-down energy loss rate $\dot{E} = 3.3 \times 10^{34}$ ergs s^{-1}. Unlike most spin-powered pulsars, Geminga is not a strong radio source. Detection of pulsed radio emission at 102 MHz was claimed by Malofeev & Malov (1997), Kuz'min & Losovskii (1997), and Shitov & Pugachev (1998), but the pulsar has not been detected at other frequencies (e.g., McLaughlin et al. 1999).

ROSAT, *Extreme Ultraviolet Explorer* (*EUVE*), and *Advanced Satellite for Cosmology and Astrophysics* (*ASCA*) observations have established that the X-ray spectrum of Geminga consists of

[1] Based on observations made with the NASA/ESA *Hubble Space Telescope*, obtained at the Space Telescope Science Institute, which is operated by the Association of Universities for Research in Astronomy, Inc., under NASA contract NAS5-26555. These observations are associated with programs GO-9182 and GO-9756.

[2] Department of Astronomy and Astrophysics, Pennsylvania State University, 525 Davey Laboratory, University Park, PA 16802; green@astro.psu.edu, pavlov@astro.psu.edu.

[3] Space Science Department, NASA Marshall Space Flight Center, SD50, Huntsville, AL 35812; vyacheslav.zavlin@msfc.nasa.gov.

[4] Department of Physics, Stanford University, Stanford, CA 94305; rwr@astro.stanford.edu.

a soft thermal component, likely emitted from the NS surface, and a nonthermal component, presumably generated in the pulsar magnetosphere (Halpern & Ruderman 1993; Halpern & Wang 1997; Jackson et al. 2002). Recent observations of Geminga with *XMM-Newton* have shown an extended emission resembling a bow-shock nebula (Caraveo et al. 2003). From a two-component, blackbody (BB) plus power law (PL) fit of the phase-integrated *XMM-Newton* spectrum, Zavlin & Pavlov (2004b) found a temperature $T_{\rm BB} \approx 0.5$ MK for the thermal component and a photon index $\Gamma \approx 2$ for the magnetospheric component. The X-ray pulse profile shows a strong dependence on energy, changing from a single broad peak at $E \lesssim 0.8$ keV to a double-peak structure at $E \gtrsim 2$ keV.

The shape of Geminga's optical spectrum remains controversial. Based on photometry with a few broadband filters, Bignami et al. (1996) proposed a broad emission feature around $\sim$5000 Å, superimposed on a Rayleigh-Jeans thermal spectrum (see also Mignani et al. 1998), and interpreted the feature as an ion cyclotron line emitted from the NS atmosphere. Martin et al. (1998) reported a possible broad dip over 6300–6500 Å in a flat ($\Gamma \approx 1.8$) spectrum spanning 3700–8000 Å, but the spectrum was severely contaminated by the sky background. Harlow et al. (1998) detected Geminga in two near-infrared (NIR) bands, which proved that the spectrum grows toward lower frequencies, similar to another middle-aged pulsar B0656+14 (Koptsevich et al. 2001). Overall, it is clear that the optical spectrum is predominantly nonthermal, perhaps with a hint of a Rayleigh-Jeans component at $\lambda \lesssim 3000$ Å. Optical pulsations of Geminga were (marginally) detected in the *B* band only (Shearer et al. 1998).

Based on three *HST* WFPC2 observations, Caraveo et al. (1996) found Geminga's parallax of 6.4 ± 1.7 mas, corresponding to $d \approx 160$ pc. Our reanalysis of these data together with a fourth WFPC2 observation shows that the result is not reliable because the exposures were too short to determine Geminga's positions with the required accuracy (G. Pavlov et al. 2005, in preparation). Therefore, the distance to Geminga is currently unknown. In this paper we scale the distance to $d = 200$ pc.

Particularly interesting would be an observation of Geminga in the far-ultraviolet (FUV) range, where one could expect thermal radiation from the NS surface to take over the apparently nonthermal radiation that prevails in the optical. Moreover, observing pulsations of Geminga shortward of $\sim$4000 Å allow one to study the transformation of the pulse profile in the transition from the nonthermal to thermal regime and elucidate the nature of Geminga's radiation in the optical-UV range. To measure the spectrum and pulsations in the ultraviolet, we carried out an imaging observation with NUV-MAMA and a spectral observation with FUV-MAMA, both with time resolution of 125 μs. These observations and the data analysis, including the NIR-optical-UV data, are described in § 2. In § 3 we present the spectral and timing analyses of a recent *XMM-Newton* observation of Geminga. Implications of the broadband (NIR through X-rays) observations are discussed in § 4. The results of our work are summarized in § 5.

2. OBSERVATIONS AND DATA ANALYSIS

2.1. *NUV-MAMA Photometry*

Geminga was observed with the STIS NUV-MAMA on 2002 February 27 (start date is 52,332.4340 MJD UT). The broadband filter F25SRF2 (pivot wavelength 2299 Å, FWHM 1128 Å) was used in this imaging observation to minimize the contribution of geocoronal lines. The data were taken during four consecutive orbits. The total scientific exposure time was 11,367 s.

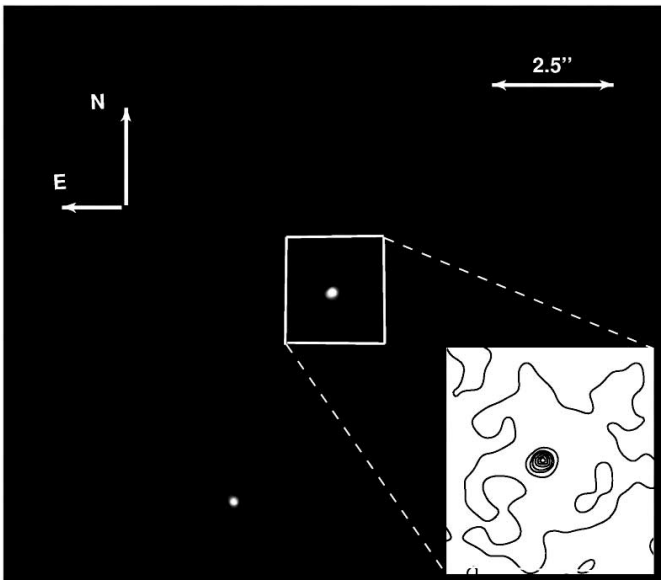

FIG. 1.—NUV-MAMA image of the field around the Geminga pulsar (at the center of the image). The only other point source in the field is star G (e.g., Halpern et al. 1985), used for acquisition. The inset shows brightness contours in the $2\farcs1 \times 2\farcs2$ region centered on Geminga.

To avoid possible additional errors associated with the pipeline subtraction of the strong dark current background (see § 7.4.2 of Kim Quijano et al. 2003), we reprocessed the "raw" NUV-MAMA images by repeating all standard calibration pipeline steps except for this subtraction. As an output, we obtained four flat-fielded, "low-resolution" images (1024×1024 pixels; plate scale $0\farcs0244$ pixel^{-1}). The target was detected in each of the four exposures. To increase the signal-to-noise ratio (S/N), we combined the images from the four exposures into a single image using the STSDAS[5] task *mscombine*. From the sharpness of the source count distributions for the two point sources detected, Geminga and star G (see Fig. 1), we conclude that the images are aligned well enough for the photometry purposes. (Slight apparent elongations of the images of the two point sources, in different directions for Geminga and star G, are likely caused by nonuniformities of the background.) We measure the background, which is dominated by the detector dark current, in the annulus with the inner radius of 40 pixels and outer radius of 55 pixels, centered on the source ($X = 539.5$ and $Y = 540.5$ pixels). The mean background count rate within the annulus is 1.59×10^{-3} counts s^{-1} pixel^{-1}.

To find an optimal aperture radius, we measured the number of source counts, $N_s = N_t - N_b$ (where N_t is the total number of counts and N_b is the number of background counts estimated by scaling the mean background in the annulus to the aperture area), and its uncertainty, δN_s, in apertures with radii of about 2, 3, 4, 5, 6, and 7 pixels (see Table 1). To evaluate the background uncertainty needed for calculating δN_s, we put each of the apertures at 15 positions randomly distributed over the annulus, measured the number of background counts within the aperture for each position, and calculated the rms, δN_b, of the differences between this number and the mean background scaled to the aperture area. The uncertainty of the source counts can then be calculated as $\delta N_s = [N_s + \delta N_b^2(1 + 1/15)]^{1/2}$ for each of the apertures. From Table 1 we see that the dependence of S/N ($=N_s/\delta N_s$) on

[5] The Space Telescope Data Analysis System is available at http://www.stsci.edu/resources/software_hardware/stsdas.

TABLE 1
NUV-MAMA Counts and Fluxes for Different Extraction Aperture Sizes

r_s[a]	N_t	N_b[b]	δN_b	N_s	δN_s	S/N	$\bar{\epsilon}$	C[c]	$\bar{F}_\lambda$[d]	$\langle F_\lambda \rangle$[d]
1.95.....	1464.7	215.4	40.2	1249.2	54.5	22.9	0.496	0.222	1.26	1.33
2.99.....	2119.6	502.7	21.8	1616.9	46.1	35.1	0.566	0.251	1.45	1.50
3.95.....	2688.3	879.7	26.1	1808.6	50.4	35.9	0.628	0.253	1.47	1.51
4.98.....	3357.4	1400.3	35.2	1957.1	57.3	34.2	0.691	0.249	1.46	1.49
5.97.....	4115.1	2010.6	35.4	2104.5	58.7	35.9	0.716	0.259	1.51	1.55
7.02.....	4950.4	2782.6	51.2	2167.8	70.5	30.8	0.741	0.257	1.50	1.53

[a] Radius of the extraction aperture in pixels.
[b] Number of background counts within the extraction aperture.
[c] Source count rate corrected for the finite aperture in counts s^{-1}.
[d] Mean spectral flux (see eqs. [2] and [3]) in units of 10^{-18} ergs cm^{-2} s^{-1} $Å^{-1}$.

aperture radius has a flat maximum at a level of S/N $\approx$ 35 at $r \approx 3$–6 pixels.

We also measured the numbers of counts in the image combined from the automatically processed images (with the dark current subtracted), performing standard aperture photometry with the IRAF task *phot* from the *apphot* package.[6] A good agreement with the results obtained from the direct measurements of the total (dark current plus sky) background (e.g., $N_s \pm \delta N_s = 1821 \pm 51$ vs. 1808 ± 50, for the 4 pixel radius aperture) shows that the pipeline subtraction of the dark current does not introduce substantial errors in this case.

The source spectral flux F_λ is connected with the number of source counts in a given aperture by the integral relation

$$N_s = t \int R_\lambda \lambda F_\lambda \epsilon_\lambda \, d\lambda, \tag{1}$$

where t is the exposure time, R_λ is the integrated system throughput, including the Optical Telescope Assembly (OTA) and filter throughputs,[7] and ϵ_λ is the wavelength-dependent encircled energy fraction. One can define the average flux in the filter passband as either

$$\bar{F}_\lambda = \frac{N_s}{t \int R_\lambda \lambda \epsilon_\lambda \, d\lambda} \tag{2}$$

or

$$\langle F_\lambda \rangle = \frac{N_s}{t \bar{\epsilon} \int R_\lambda \lambda \, d\lambda}, \tag{3}$$

where $\bar{\epsilon}$ is in average encircled energy fraction in the filter passband and $N_s/(t\bar{\epsilon}) = C$ is the source count rate corrected for the finite aperture. We calculated the average spectral fluxes in both ways (see Table 1) using the ϵ_λ-values measured by Proffitt et al. (2003) for several aperture radii. We see that the mean fluxes, $\bar{F}_\lambda \simeq \langle F_\lambda \rangle \simeq 1.5 \times 10^{-18}$ ergs cm^{-2} s^{-1} $Å^{-1}$, are close to each other for $r \gtrsim 3$ pixels. The uncertainty of these values, $\sim$10%, is mostly due to systematic errors in the encircled energy fraction.

Another way to evaluate the flux is to assume some shape for the spectral flux F_λ and determine its normalization using equation (1). We approximate the spectral flux in the F25SRF2 passband as an absorbed power law: $F_\lambda = F_{2299}(\lambda/2299\ Å)^{\alpha_\lambda} \times 10^{-0.4A(\lambda)E(B-V)}$, where F_{2229} is the intrinsic source spectral flux at the pivot wavelength [it coincides with $\bar{F}_\lambda$ in the special case $\alpha_\lambda = 0$, $E(B-V) = 0$] and $A(\lambda)$ is the ultraviolet extinction curve (Seaton 1979). The color index $E(B-V)$ is poorly known. An estimate based on the hydrogen column density found from the X-ray fits (see § 3.1) gives $E(B-V) \simeq 0.03$; below we adopt $E(B-V) = 0.01$–0.07 as a plausible range. We calculated the dependences of F_{2299} on the spectral slope α_λ in a reasonable range $-4 \le \alpha_\lambda \le 0$ for several values of $E(B-V)$, based on the N_s-values measured in the 4 pixel radius aperture (see Fig. 2). We see that, at a given $E(B-V)$, F_{2299} varies with α_λ by up to 20%. We estimate the uncertainty of the F_{2299}-values at given α_λ and $E(B-V)$ as $\approx$8%–10%, mostly associated with changes of the MAMA imaging point spread function (PSF) between individual observations that cause systematic uncertainties of ϵ_λ (see Proffitt et al. [2003] and § 16.1 of Kim Quijano et al. [2003]).

2.2. *FUV-MAMA Spectrum*

Geminga was observed with the STIS FUV-MAMA on 2002 February 26 (start date is 52,331.2391 MJD UT). The low-resolution grating G140L (which covers the wavelength interval $\approx$1150–1700 Å) with the $52'' \times 0\farcs5$ slit was used. The data were taken during four consecutive orbits (including the target acquisition). We used a nearby field star G ($V = 21.3$, Fig. 1) as the acquisition target and applied a $4\farcs9$ offset, deduced from the positions of Geminga and the acquisition star measured in the

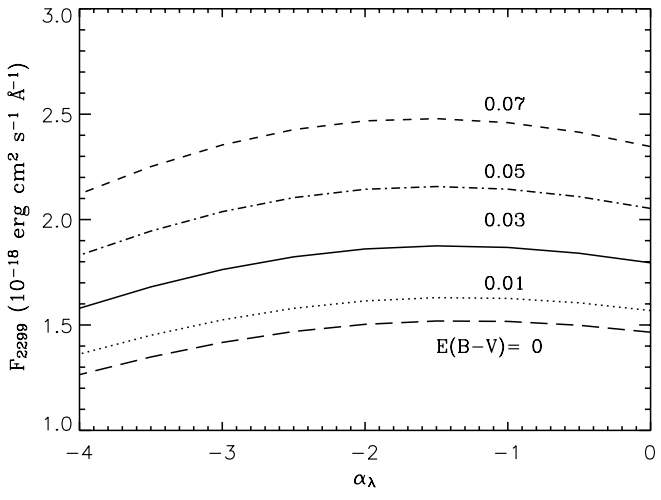

Fig. 2.—Spectral flux F_λ at $\lambda = 2299$ Å as a function of spectral slope α_λ in the NUV-MAMA F25SRF2 band, for different values of $E(B-V)$.

[6] See http://stsdas.stsci.edu/cgi-bin/gethelp.cgi?phot.hlp.
[7] We corrected the throughputs supplied with the data for the time-dependent sensitivity loss (see http://www.stsci.edu/hst/stis/calibration/reference_files/tds.html).

FIG. 3.—Raw FUV-MAMA spectrum of Geminga. The boxes show approximate regions for the source and background extraction used in spectral analysis.

archival *HST* images, which placed Geminga about 0.″1 off the slit center. The total scientific exposure time was 10,674 s.

For each exposure, we processed the raw "high-resolution" images (2048×2048 pixels, plate scale of 0.″0122 pixel^{-1}—see § 11 of Kim Quijano et al. 2003) using the calibration files available on 2003 July 1. As an output, we obtained flat-fielded, low-resolution (1024×1024 pixels, plate scale 0.″0244 pixel^{-1}, spectral resolution 0.58 Å pixel^{-1}) images and used them for the spectral analysis.

The processed images show a nonuniform detector background that consists of a flat (constant) component and the so-called thermal glow component (Landsman 1998) that dominates over most of the detector area and grows with increasing the temperature of the FUV-MAMA low-voltage power supply (LVPS; the average LVPS temperatures were 38.45°C, 39.67°C, 40.89°C, and 41.62°C in the four consecutive orbits of our observation). The thermal glow is the strongest in the upper-left quadrant of the detector, where the dark count rate can exceed the nominal value, 6×10^{-6} counts s^{-1} pixel^{-1}, by a factor of 20. To reduce the contamination caused by the thermal glow background, the source was placed close to the bottom edge of the detector (see Fig. 3).

We find Geminga's spectrum centered at $Y = 105 \pm 2$ pixels in each of the flat-fielded images (the centroid position slightly varies with X), where X and Y are the image coordinates along the dispersion and spatial axes, respectively. Even at this location on the detector the background still exceeds the nominal value by a factor of 1.5–5, depending on the position along the dispersion axis. To improve S/N, we combined the images from four exposures into a single image using the STSDAS task *mscombine*. The Y-positions of the centroids differ by less than 3 pixels for different exposures and different wavelengths (X-positions).

Accurate subtraction of the enhanced, nonuniform background [typical values are $(1–3) \times 10^{-5}$ counts s^{-1} pixel^{-1}] is crucial to measuring the spectrum of our faint target. The spectral extraction algorithm implemented in the standard STIS pipeline (task X1D) does not adequately correct for the nonuniform background while extracting the spectrum of such a faint source and does not allow variation of the extraction box size with the position along the dispersion axis. Therefore, we used an IDL routine with additional capabilities of grouping and fitting the background and selecting an optimal extraction box size depending on the position along the dispersion axis (see Kargaltsev et al. 2004).

Since the source spectrum occupies only a small region on the detector, we do not attempt to subtract the background globally. Instead, we scan the count distribution within two strips, $36 \leq Y \leq 95$ and $116 \leq Y \leq 175$, adjacent to the source region, $96 \leq Y \leq 115$. To obtain the spectrum with a sufficiently high S/N, we have to bin the spectrum heavily; after some experimenting, we chose 12 spectral bins (λ bins; see Table 2). The bins exclude the regions contaminated by the geocoronal emission (Lyα line and O I lines at 1304 and 1356 Å) and by an artificial background structure at $\lambda \approx 1379–1384$ Å, $Y \approx 96–103$. The bins outside the contaminated regions were chosen to have comparable S/N (≈6–8), whenever possible.

TABLE 2
FUV-MAMA COUNTS AND FLUXES IN λ BINS

λ Bin (Å)	A_s[a]	N_t	N_b	δN_b	N_s	δN_s	S/N	$\langle F_\lambda \rangle \pm \delta\langle F_\lambda \rangle$[b]
1155–1187	9	238.3	157.3	17.2	81.1	19.9	4.1	13.8 ± 3.4
1248–1259	9	130.7	63.6	5.39	67.1	9.9	6.8	9.5 ± 1.4
1260–1270	9	110.9	50.7	5.23	60.2	9.5	6.4	7.6 ± 1.2
1271–1283	9	132.9	54.0	4.97	78.9	10.3	7.7	9.8 ± 1.3
1316–1332	7	130.3	57.2	8.14	73.1	12.0	6.1	7.1 ± 1.2
1333–1347	11	145.8	67.5	8.66	78.3	12.6	6.2	8.2 ± 1.3
1365–1378	11	96.6	49.3	7.11	47.3	10.1	4.7	5.3 ± 1.1
1385–1402	11	123.6	62.0	4.82	61.6	9.3	6.6	6.8 ± 1.0
1403–1431	5	112.5	42.6	6.35	69.9	10.6	6.6	6.3 ± 1.0
1432–1471	5	155.8	53.1	6.98	102.8	12.4	8.3	7.7 ± 0.9
1472–1525	5	140.1	61.3	8.01	78.9	12.1	6.5	6.0 ± 0.9
1526–1702	5	258.5	155.1	9.39	103.4	14.0	7.4	5.1 ± 0.7
Summed[c]	...	1776.0	873.6	28.8	902.5	42.3[d]	20.9	6.76 ± 0.43[e]

[a] Height of extraction box in pixels.
[b] Average spectral flux and its statistical error, in units of 10^{-18} ergs s^{-1} cm^{-2} Å^{-1}, corrected for the finite aperture.
[c] Values for summed λ bins.
[d] Defined as $[\sum_i (\delta N_{s,i})^2]^{1/2}$.
[e] Defined as $[\sum_i \langle F_\lambda \rangle \Delta\lambda_i \pm (\sum_i \langle \delta F_\lambda \rangle_i^2 \Delta\lambda_i^2)^{1/2}](\sum_i \Delta\lambda_i)^{-1}$.

For each of the λ bins, we calculate the total number of counts, N_t, within the extraction boxes of different heights (one-dimensional apertures): $A_s = 3, 5, 7, 9, 11, 13, 15$, and 17 pixels, centered at $Y = 106$ for the first two λ bins and at $Y = 105$ for the rest of the λ bins. To evaluate the background, we first clean the background strips (see above) from outstanding ($>10^{-3}$ counts s^{-1} $pixel^{-1}$) values ("bad pixels") by setting them to local average values. Then for each of the λ bins, we fit the Y-distribution of the background counts with a first-order polynomial (interpolating across the source region), estimate the number N_b of background counts within the source extraction aperture A_s, and evaluate the number of source counts, $N_s = N_t - N_b$ (Table 2).

The uncertainty δN_s of the source counts can be evaluated as $\delta N_s = [N_s + \delta N_b^2(1 + A_s/A_b)]^{1/2}$, where δN_b is the background uncertainty in the source aperture. We binned the distribution of background counts along the Y-axis with the bin sizes equal to A_s and calculated δN_b as the rms of the differences between the actual numbers of background counts in the bins and those obtained from the fit to the background. We calculated δN_s and S/N for various extraction box heights and found the A_s-values maximizing S/N for each λ bin (see Table 2).

We calculated the average spectral fluxes in the λ bins (cf. eq. [3]),

$$\langle F_\lambda \rangle_i = \frac{\int_{\Delta\lambda_i} R_\lambda \lambda F_\lambda \, d\lambda}{\int_{\Delta\lambda_i} R_\lambda \lambda \, d\lambda} = \frac{C_i}{\int_{\Delta\lambda_i} R_\lambda \lambda \, d\lambda}, \quad (4)$$

where C_i is the source count rate in the ith λ bin corrected for the finite size of the source extraction aperture and R_λ is the system response that includes the OTA throughput and accounts for the grating and slit losses and time-dependent sensitivity losses (Bohlin, 1999; see also § 3.4.12 of Brown et al. 2002 for details). The resulting flux values are given in Table 2, while the spectrum is shown in Figure 4. The total flux in the 1155–1702 Å range ($\Delta\lambda = 547$ Å) can be estimated as $F \simeq \Delta\lambda(\sum_i \langle F_\lambda \rangle_i \Delta\lambda_i)(\sum_i \Delta\lambda_i)^{-1} \simeq (3.72 \pm 0.24) \times 10^{-15}$ ergs s^{-1} cm^{-2}, corresponding to the luminosity $L_{\rm FUV} = 4\pi d^2 F = (1.78 \pm 0.11) \times 10^{28} d_{200}^2$ ergs s^{-1}.

We fit the spectrum with the absorbed power-law model, $F_\lambda = F_{1500}(\lambda/1500\ \text{Å})^{\alpha_\lambda} \times 10^{-0.4A(\lambda)E(B-V)}$. For plausible values $E(B - V) = 0.01$, 0.03, 0.05, and 0.07, we found the power-law indices $\alpha_\lambda = -3.29 \pm 0.53$, -3.43 ± 0.53, -3.56 ± 0.54, and -3.69 ± 0.54 and the normalizations $F_{1500} = 5.38 \pm 0.33$, 6.25 ± 0.38, 7.26 ± 0.37, and $8.44 \pm 0.52 \times 10^{-18}$ ergs cm^{-2} s^{-1} $Å^{-1}$, respectively (Fig. 5); the corresponding χ^2_ν-values are 0.80, 0.81, 0.82, and 0.83, for 10 degrees of freedom (dof).

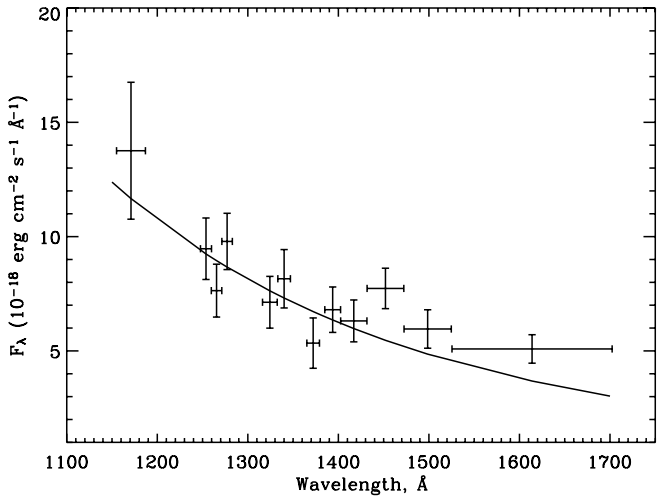

FIG. 4.—Measured (absorbed) FUV-MAMA spectrum of Geminga. The solid curve shows the best-fit absorbed blackbody model for $E(B - V) = 0.03$ ($T = 0.31$ MK at $R = 13 d_{200}$ km).

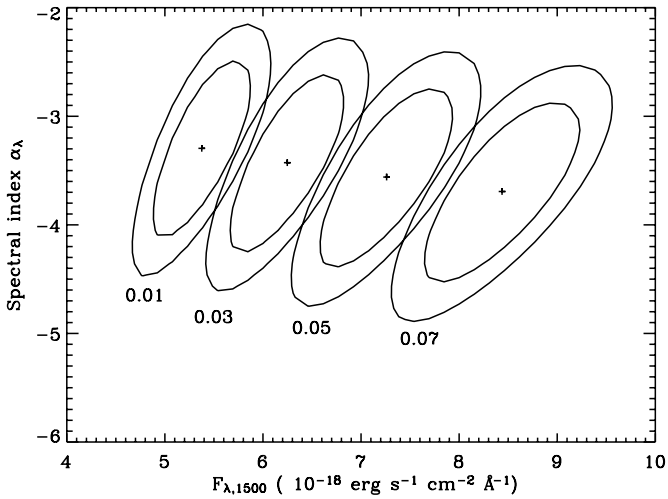

FIG. 5.—Confidence contours (67% and 90%) for the absorbed power-law model fit to the FUV-MAMA spectrum, for $E(B - V) = 0.01$, 0.03, 0.05, and 0.07.

The inferred slope α_λ is close to that of the Rayleigh-Jeans spectrum $F_\lambda \propto \lambda^{-4}$, suggesting that the observed radiation is dominated by thermal emission from the NS surface. To estimate the NS surface temperature, we fit the absorbed blackbody model to the observed spectrum. Since the FUV fluxes are in the Rayleigh-Jeans part of the spectrum, the temperature is strongly correlated with the radius-to-distance ratio (approximately $T \propto d^2/R^2$), as demonstrated by the confidence contours in the T-R plane (Fig. 6). For a typical NS radius $R = 13$ km and the assumed distance $d = 200$ pc, the inferred surface temperatures are 0.27 ± 0.01, 0.31 ± 0.01, 0.36 ± 0.02, and 0.41 ± 0.02 MK, for $E(B - V) = 0.01$, 0.03, 0.05, and 0.07, respectively; the corresponding χ^2_ν-values are 0.90, 0.87, 0.85, and 0.85, for 10 dof. An example of best-fit blackbody spectrum is shown in Figure 4, for $E(B - V) = 0.03$.

2.3. *NIR through FUV Spectrum*

To compare the UV emission of Geminga with its NIR-optical emission, we plot in Figure 7 the FUV-MAMA and NUV-MAMA spectral fluxes $\langle F_\nu \rangle$ together with the fluxes at lower frequencies measured in eight broad passbands. Seven of these fluxes have been published previously (see caption to Fig. 7 for references), while the flux marked "555W" in Figure 7 was measured in this work from a recent observation of Geminga with the *HST* Advanced Camera for Surveys (ACS).

Geminga was observed with the Wide Field Channel (WFC) of the ACS on 2003 October 7 for 6296 s total exposure (three *HST* orbits, two dither positions per orbit, two exposures per dither position) in the F555W filter (ACS "V filter"; pivot wavelength 5358 Å, FWHM 1235 Å). We combined the aligned, pipeline-calibrated images from the three orbits into a single image and performed aperture photometry using the *phot* task from the IRAF *apphot* package. To extract the source counts, we used a circular aperture with a radius of $0''.15$ (3 WFC pixels), which provides an optimal S/N ≈ 36. For this aperture, the encircled energy fraction of 0.82 ± 0.04 was determined from the empirical PSF measured for six field stars with apertures varying from 2 to 25 WFC pixels. The source count rate was

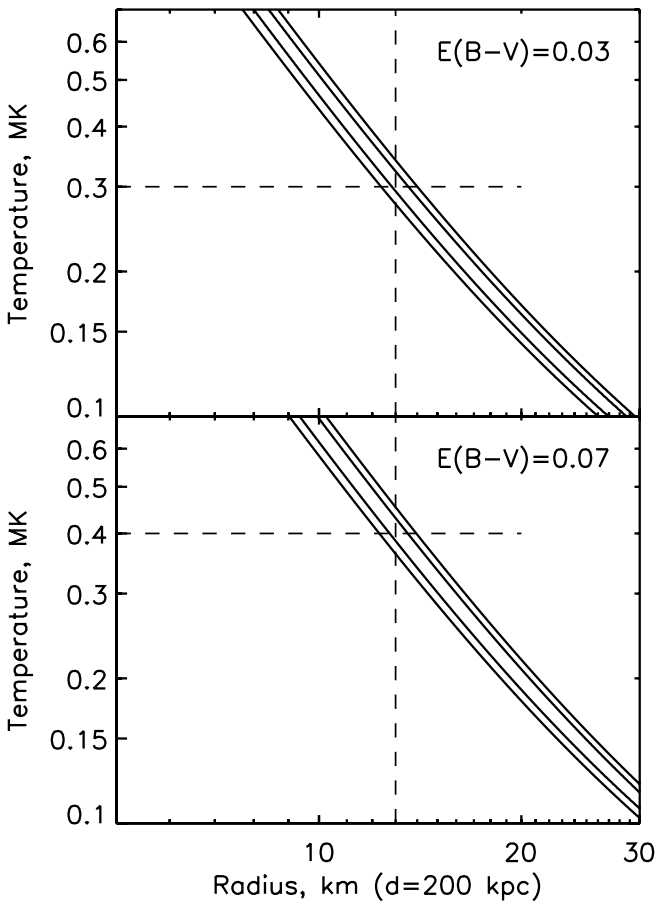

FIG. 6.—Confidence contours (67% and 99%) for the absorbed blackbody model fit to the FUV-MAMA spectrum, for $E(B-V)=0.03$ and 0.07.

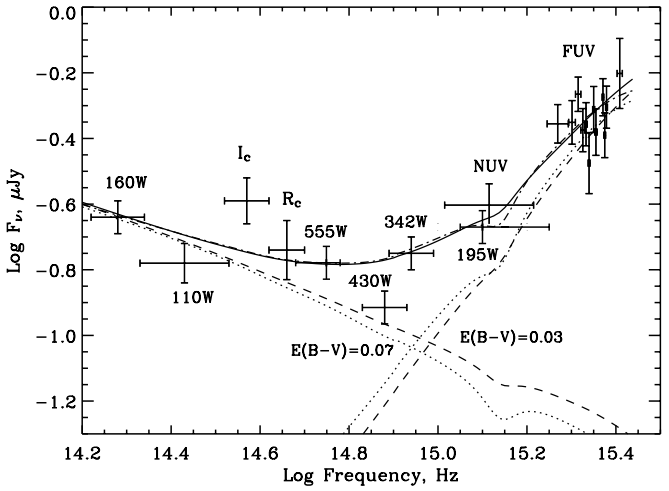

FIG. 7.—NIR through FUV spectrum of Geminga. The broadband fluxes were measured with the *HST* NICMOS (F110W and F160W; Koptsevich et al. 2001), Subaru SuprimeCam (I_C and R_C; Komarova et al. 2003), *HST* ACS WFC (F555W; this work), and *HST* Faint Object Camera (FOC) (F430W, F342W, and F195W; Bignami et al. 1996; Mignani et al. 1998). The solid and dash-dotted lines show the fits with the absorbed blackbody plus power-law model for $E(B-V)=0.03$ and 0.07, respectively. The model components are shown by the dashed and dotted lines (see text for details).

corrected for the finite aperture size and converted to average spectral flux (cf. eq. [3]) using the conversion factor (inverse sensitivity), 1.974×10^{-19} ergs cm^{-2} Å^{-1} count^{-1}, for this observing mode.[8] The accuracy of the flux measurement, about 10%, is limited by the uncertainty in the encircled energy fraction and various systematic uncertainties. The flux we measured, $\langle F_\nu\rangle = 0.17 \pm 0.02$ μJy, is a factor of 1.6 lower than that measured by Bignami et al. (1996) from the *HST* WFPC2 observation of 1994 September 23 with a similar filter. We remeasured the WFPC2 F555W flux and obtained a value consistent with our ACS result within the uncertainties. With the new value for the F555W flux and the other NIR-optical fluxes, we conclude that the "cyclotron feature" in Geminga's spectrum (Bignami et al. 1996; Mignani et al. 1998) was likely a result of inaccurate photometry.

It is obvious from Figure 7 that the NIR through FUV spectrum of Geminga cannot be described by a simple power-law model. We fit this spectrum with a two-component, power law plus blackbody model. Since the temperature and the radius-to-distance ratio of the blackbody component are strongly correlated in the Rayleigh-Jeans regime ($TR^2/d^2 \approx$ constant), we have to fix one of these parameters in the fit. For the fixed $R/d = 13$ km/200 pc, we obtained $T = 0.30 \pm 0.02$ MK, $\alpha_\nu = -0.46 \pm 0.12$, and $F_0 = 0.11 \pm 0.02$ μJy for $E(B-V)=0.03$ and $T = 0.41 \pm 0.02$ MK, $\alpha_\nu = -0.41 \pm 0.13$, and $F_0 = 0.12 \pm 0.02$ μJy for $E(B-V)=0.07$ ($\chi^2_\nu = 1.5$ for 18 dof for each of the fits), where α_ν and F_0 are the parameters of the power-law component: $F_\nu = F_0[\nu/(10^{15}\ \mathrm{Hz})]^{\alpha_\nu}$. Notice that the parameters of the blackbody component are virtually the same as those obtained from the FUV-MAMA spectrum alone. The best-fit spectra and their components are shown in Figure 7. We see that the blackbody emission dominates at $\nu \gtrsim 1\times10^{15}$ Hz ($\lambda \lesssim 3000$ Å), while the power-law (presumably magnetospheric) emission dominates at longer wavelengths.

2.4. *Timing Analysis*

For the timing analysis of the NUV-MAMA and FUV-MAMA data, we used the so-called TIME-TAG data files that contain the photon arrival times, recorded at a 125 μs time resolution, and high-resolution detector coordinates (see § 2.2) associated with each of the events. We use 2688 NUV-MAMA events extracted from an aperture of 8 high-resolution pixels radius (includes 66% of source counts) and 1939 FUV-MAMA events extracted from the above-defined λ bins with heights of extraction boxes varying from 14 to 22 high-resolution pixels, depending on the λ bin (includes 46% of source counts). The arrival times are corrected for the Earth and spacecraft motions and transformed to barycentric dynamical times (TDB) at the solar system barycenter using the STSDAS task *odelaytime*. The time spans of the FUV-MAMA and NUV-MAMA observations are 19,181 and 19,785 s, respectively, with a gap of 84,041 s between the last FUV-MAMA event and the first NUV-MAMA event.

The expected frequency of Geminga's pulsations at the epoch of our observation, around 52,332 MJD, can be estimated from the previous timing observations in γ-rays and X-rays. The most recent ephemerides of Geminga were published by Jackson et al. (2002; hereafter J02). These authors found a small glitch in Geminga's timing history and presented a postglitch ephemeris for a time interval of 50,382–51,673 MJD. Although our observation was taken 659 days after the end of that interval, extrapolation of this ephemeris to 52,332 MJD predicts the frequency, $f_{\mathrm{J02}} = 4,217,608.6953$ μHz, with a formal uncertainty of ±0.0013 μHz, which is about 3 orders of magnitude

[8] See http://www.stsci.edu/hst/acs/documents/handbooks/DataHandbookv2/intro_ch34.html#1896082.

smaller than what we can achieve in our relatively short observation (see below). Therefore, we adopt f_{J02} as an estimate of expected frequency and look for pulsations in its vicinity in a $f_{J02} \pm (2T_{span})^{-1}$ frequency range.

Since the longer time span, $T_{span} = 123,005$ s, of the joint FUV+NUV data set allows a tighter constraint on the pulsation frequency, we start from the analysis of this data set. First, we apply the Z_n^2-test (Buccheri et al. 1983), calculating the Z_n^2-statistic as a function of trial frequency in the range of $f_{J02} \pm 4$ μHz for $n = 1$–8, where n is the number of harmonics included. For each of the n-values examined, we found statistically significant pulsations, with frequencies of Z_n^2 maxima within $(-0.3, +0.7)$ μHz around f_{J02}. The most significant result is obtained for $n = 6$: maximum $Z_6^2 = 53.1$ at $f = 4{,}217{,}608.8$ μHz; the probability to obtain this value by chance is 4×10^{-7}. To better estimate the uncertainty of pulsation frequency, we also applied the odds-ratio method of Gregory & Loredo (1996; see also Zavlin et al. 2004) and found $f = 4{,}217{,}608.3^{+0.7}_{-0.9}$ μHz for the median frequency and 68% uncertainties and $f = 4{,}217{,}608.8 \pm 1.2$ μHz for the mean frequency and standard deviation. Within the uncertainties, these frequencies virtually coincide with the frequency predicted by the J02 ephemeris. The expected frequency shift during the FUV+NUV observation, $\dot{f} T_{span} = 0.024$ μHz, is much smaller than the frequency uncertainties in our measurement, which means that this observation is not sensitive to frequency derivative $\dot{f}$.

Since our spectral analysis has shown that the FUV radiation is predominantly thermal, while the NUV radiation has a significant contribution from the magnetospheric component (see § 2.3 and Fig. 7), one can expect different strength and shape of pulsations in the FUV and NUV bands. Therefore, we analyzed these two data sets separately. Since the frequency that we measured from the FUV+NUV data is consistent with the J02 ephemeris, and an *XMM-Newton* observation taken 37 days later also suggests that the ephemeris may still be valid (see § 3.2), we folded the times of arrival with the J02 ephemeris, choosing the same zero-phase epoch, 50,382.999999364 MJD.

The folded (source plus background) light curve in the NUV-MAMA band, plotted in the top panel of Figure 8, shows one broad (FWHM ≈ 0.8 in phase), flat-top peak per period, centered at $\phi \approx 1.0$. The most notable feature of the pulse profile is the narrow dip at $\phi \approx 0.45$. The Z_n^2-test shows that the pulsations are statistically quite significant, with the main contribution coming from the fundamental frequency: $Z_1^2 = 22.3$ corresponds to 1×10^{-5} probability of false result. The pulsed fraction, defined as the ratio of the number of counts above the minimum level to the total number of counts in the light curve, is about 28%, which corresponds to the intrinsic source pulsed fraction $f_p \approx 40\%$.

The Z_n^2-test for the FUV-MAMA data set shows most significant pulsations for $n = 4$: $Z_4^2 = 25.08$ corresponds to 99.84% (3.2 σ) significance. The lower significance of the FUV pulsations, compared to the NUV pulsations, can be caused by a lower S/N in the spectroscopic mode. Since the thermal-glow background was growing with increasing LVPS temperature in the course of our observation (see § 2.2), we performed the timing analysis for various combinations of orbits and found that indeed the pulsations were more significant in earlier orbits. For instance, in the first two orbits ($T_{span} = 7638$ s, $N = 844$ counts) the most significant $Z_2^2 = 23.46$ corresponds to 99.990% (3.9 σ) significance.

The four-orbit and two-orbit FUV-MAMA light curves are shown in the middle and bottom panels of Figure 8. In the same panels we show the light curves for the background counts extracted from two boxes centered at $Y = 180$ and $Y = 240$ high-resolution pixels, with the same heights as those used for extraction of the source events. The background light curves do not show statistically significant pulsations. Both the four-orbit and two-orbit source-plus-background light curves show a sharp, asymmetric dip at approximately the same phase as the NUV-MAMA light curve. A hint of a shallower dip, better pronounced

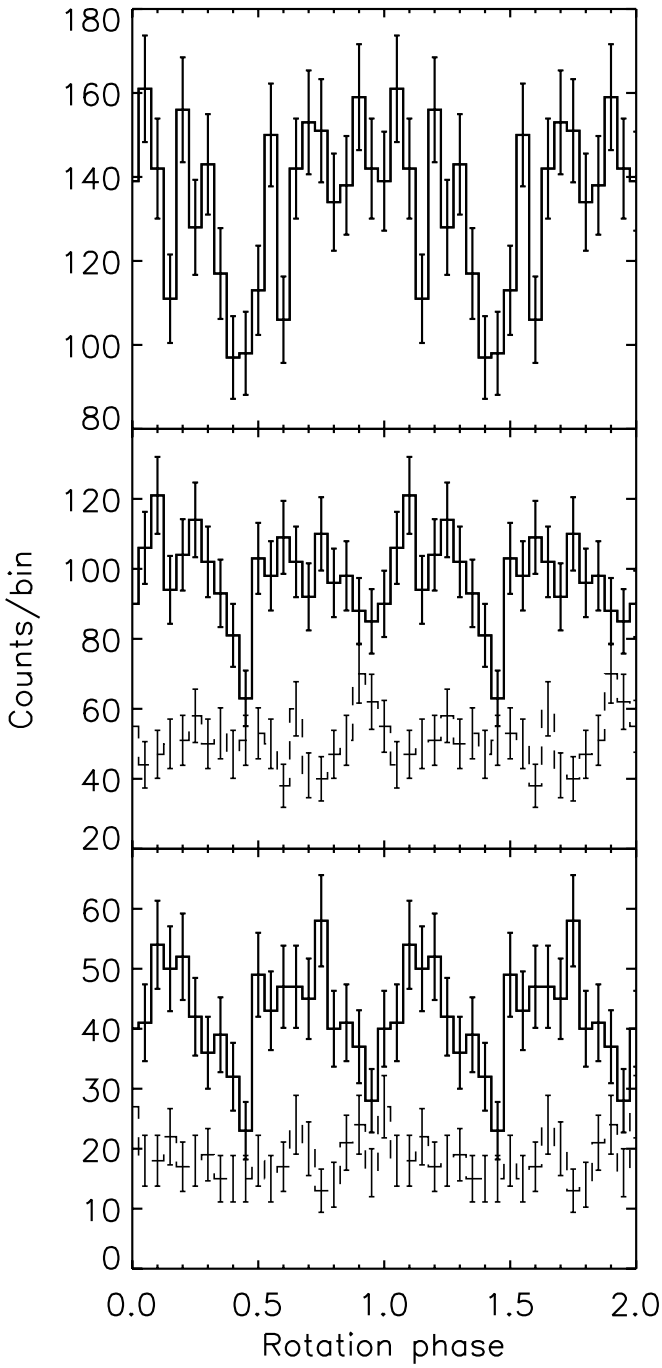

FIG. 8.—UV light curves of Geminga folded with the J02 ephemeris. *Top*: NUV-MAMA light curve, obtained using the data from all four orbits. The estimated average background level in the 20 bin light curve is 44.3 counts per phase bin. *Middle*: FUV-MAMA light curve, obtained using the data from all four orbits. *Bottom*: FUV-MAMA light curve, obtained using only the data from the first two orbits. The dashed lines with associated error bars show the corresponding background light curves (see text).

in the two-orbit light curve, is seen at $\phi \approx 0.95$. The pulsed fraction in the observed (source + background) radiation is about 35% and 45% for the four orbits and first two orbits, respectively. The corresponding intrinsic pulsed fractions are rather high, about 60%–70%. It should be noted, however, that these values are rather uncertain because of the large statistical error of the minimum level.

3. X-RAY SPECTRUM AND PULSATIONS OF GEMINGA

To better understand the UV spectrum and pulsations of Geminga, observations at X-ray wavelengths are particularly useful. The deepest observation of Geminga in X-rays was carried out with the *XMM-Newton* observatory on 2002 April 4–5 (orbit 425). The European Photon Imaging Camera (EPIC) MOS and pn instruments observed the pulsar for 101.4 and 71.4 ks of effective exposures, respectively. Two EPIC MOS detectors were operated with medium filters in full frame mode, providing an image of a large area, $r \sim 14'$, with time resolution of 2.6 s. EPIC pn was used in combination with thin filter in small window mode that covers a $4\farcm37 \times 4\farcm37$ region and provides a 5.7 ms time resolution. First results of this observation have been reported by Zavlin & Pavlov (2004b) and Caraveo et al. (2004a, 2004b). Here we briefly describe the X-ray spectrum and pulsations of Geminga, with emphasis on the properties most useful for the comparison with the optical-UV data.

3.1. *X-Ray Spectrum*

The most detailed X-ray spectrum of Geminga was obtained with the EPIC pn instrument. The EPIC pn data, processed with the SAS package (ver. 6.0.0),[9] were used for the spectral and timing analysis. We extracted the source (plus background) photons from a $40''$ radius circle centered at the pulsar position, which contains about 88% of source counts. The estimated total source count rate (corrected for finite extraction radius) is 0.813 ± 0.004 counts s^{-1} in the 0.2–10 keV range for single and double events (with photon-induced charge detected in a single CCD pixel and two adjacent pixels). The 0.2–10 keV phase-integrated spectrum was binned in 222 spectral bins with at least 40 source counts per bin. The detector response matrix and effective area were generated with the *rmfgen* and *arfgen* tools, respectively. Fitting this spectrum with a two-component, blackbody (BB) plus power-law (PL), model, we find the blackbody temperature $T_{\rm BB} = 0.47 \pm 0.02$ MK and radius $R = (17.0 \pm 2.5)\,d_{200}$ km, which suggests that the thermal component originates from the NS surface. The PL component, with a photon index $\Gamma = 2.02 \pm 0.05$, dominates at energies $E \gtrsim 0.6$ keV and contains about 10% of the total luminosity in the 0.2–10 keV band, $L^{\rm pl}_{0.2-10\,{\rm keV}} = (2.6 \pm 0.1) \times 10^{30}\, d^2_{200}$ ergs s^{-1} $\simeq 7 \times 10^{-5} d^2_{200} \dot{E}$. Extrapolated into the optical domain, the PL component exceeds the observed optical fluxes by a factor of 100–500, which might be interpreted as a flattening of the pulsar magnetospheric spectrum at lower photon energies. The hydrogen column density derived from this fit is $n_{\rm H} = (2.9 \pm 0.2) \times 10^{20}$ cm^{-2}.

Although the two-component model cannot be rejected based on the overall fit quality ($\chi^2_\nu = 1.11$ for 217 dof; systematic errors in the EPIC pn response not included), the fit residuals show some excess of observed counts over the best-fit model at higher energies, $E \gtrsim 7$ keV, indicating a harder PL spectrum. Indeed, fitting the high-energy tail ($E > 2.5$ keV) of the spectrum with a single PL model gives $\Gamma = 1.56 \pm 0.24$ and $L^{\rm pl}_{0.2-10\,{\rm keV}} = (2.2 \pm 0.2) \times 10^{30}\, d^2_{200}$ ergs s^{-1} ($\chi^2_\nu = 0.98$ for 30 dof). The BB+PL fit with Γ fixed at this value is statistically unacceptable ($\chi_\nu = 2.95$ for 219 dof). Therefore, we tried a three-component model consisting of soft (TS) and hard (TH) blackbody components and a PL component. With the PL parameters fixed at the values obtained from the best PL fit in the 2.5–10 keV band ($\Gamma = 1.56, \mathcal{N} = 5.5 \times 10^{-5}$ photons cm^{-2} s^{-1} keV^{-1} at 1 keV), we obtain the following parameters for the thermal components: $T_s = 0.49 \pm 0.01$ MK, $R_s = (12.9 \pm 1.0)\,d_{200}$ km, $T_h = 2.32 \pm 0.08$ MK, $R_h = (46 \pm 12)\,d_{200}$ m, and $n_{\rm H} = (2.4 \pm 0.2) \times 10^{20}$ cm^{-2} ($\chi^2_\nu = 1.10$ for 217 dof). Fitting the EPIC MOS spectra obtained in this observation yields almost the same model parameters (discarding the EPIC MOS events below 0.3 keV, where the responses of the MOS detectors are known very poorly).

In the TS+TH+PL model the TS component can be interpreted as emission from the bulk of NS surface, the TH component can be ascribed to emission from smaller, hotter regions of the NS surface, and the PL component represents the magnetospheric radiation. Such an interpretation of Geminga's X-ray spectrum is in line with the results obtained from *Chandra* and *XMM-Newton* observations of the other bright middle-aged pulsars, B0656+14 and B1055−52, whose X-ray spectra can also be described by the TS+TH+PL model with similar parameters (Pavlov et al. 2002; Zavlin & Pavlov 2004b). However, the effective radius of Geminga's TH component is much smaller than those of B0656+14 and B1055−52, about $0.6(d/0.3$ kpc) and $0.4(d/0.7$ kpc) km, respectively.

The confidence contours for the temperature and radius of the TS component are shown in Figure 9. In the same figure we plotted the temperature-radius confidence contours obtained from the blackbody fit of the FUV-MAMA spectrum for $E(B-V) = 0.03$ and 0.07 (see § 2.2 and Fig. 6). We see that at plausible values of interstellar extinction, $E(B-V) \lesssim 0.07$, the FUV contours lie at smaller radii (or lower temperatures) than the X-ray contours. This means that the extrapolation of the

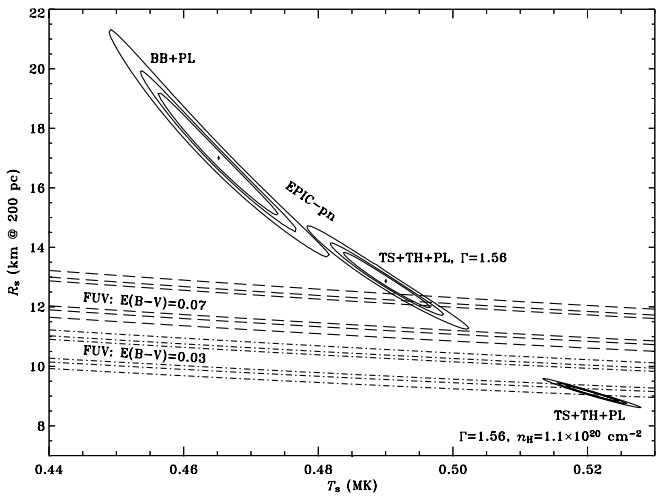

FIG. 9.—Confidence contours (68%, 90%, and 99%) in the temperature-radius plane obtained from fitting the EPIC pn spectra (*solid lines*) with the TS+TH+PL and BB+PL models (labels near the contours). The TS+TH+PL contours were obtained at the fixed parameters of the PL component; $n_{\rm H}$ was free for the upper contours, while it was fixed at the value obtained from *ROSAT* data for the lower contours. All the model parameters were free for the EPIC pn BB+PL contours. The dashed and dash-dotted lines show the confidence contours obtained from fitting the FUV-MAMA spectrum with a blackbody model for two values of the color index $E(B-V)$.

[9] Available at http://xmm.vilspa.esa.es.

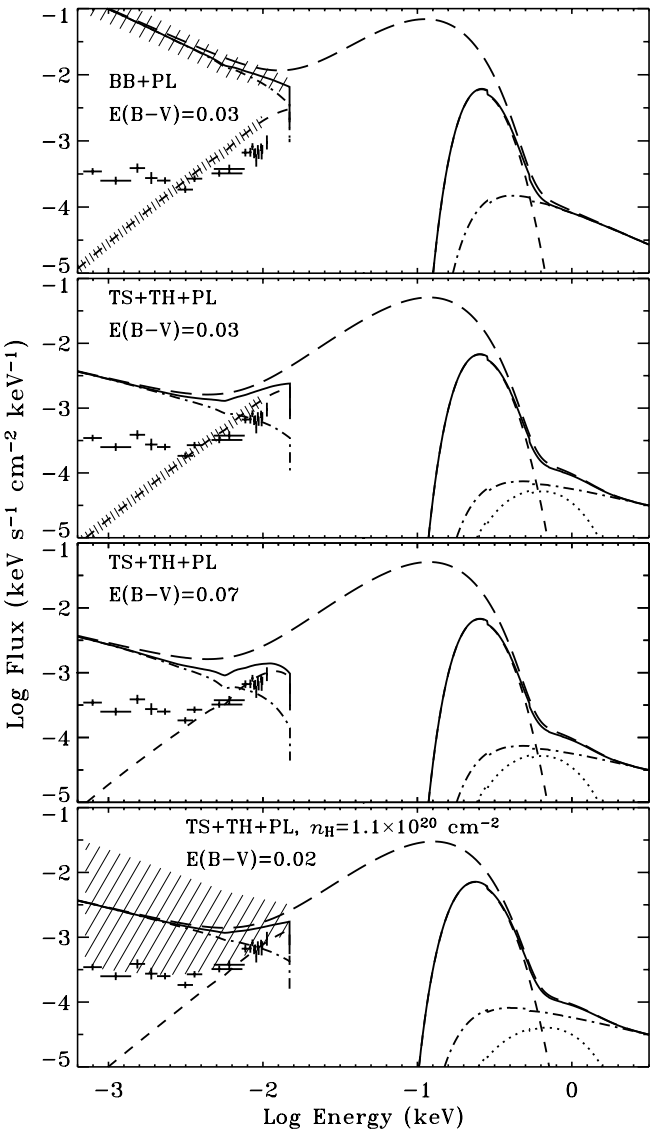

FIG. 10.—NIR through X-ray spectrum of Geminga for different X-ray spectral models and different color indices. The solid lines show the best-fit (absorbed) spectra in the X-ray range and their extrapolations into the NIR-FUV range. The short-dashed and dash-dotted lines show the (soft) thermal and PL components, respectively, the dotted lines in three bottom panels show the TH component (its contribution is negligible in the NIR-FUV range), and the long-dashed lines present the unabsorbed total spectra. The crosses depict the measured NIR-FUV spectral fluxes (cf. Fig. 7). The hatched areas along the PL and thermal components in the NIR-FUV range demonstrate propagated uncertainties of the corresponding extrapolations. The top panel shows a two-component (BB+PL) X-ray fit, while three bottom panels show TS+TH+PL fits with fixed parameters of the PL component. The fit shown in the bottom panel was obtained at a fixed n_H-value, while n_H was a fitting parameter in three top panels. (See text for more details.)

thermal X-ray component into the UV-optical goes above the observed FUV flux: $(TR^2)_X/(TR^2)_{FUV} \simeq 1.8$, 1.6, 1.4, and 1.2 for $E(B-V) = 0.01$, 0.03, 0.05, and 0.07, respectively, for the best-fit parameter values (see also Fig. 10). Such behavior is in contrast to other neutron stars observed in both X-rays and optical, for which such an extrapolation usually *underpredicts* the optical-UV fluxes[10] by a factor of 2–7 (see § 4.1). To obtain a similar ratio for Geminga, one would have to assume unrealistically high extinction, $E(B-V) \sim 0.2$–0.4.

[10] A possible exception is the Vela pulsar (see Romani et al. 2005).

If we adopt the above-described two-component (BB+PL) model, the discrepancy between the X-ray and FUV temperature and radius is even more pronounced, as demonstrated by the corresponding confidence contours in the upper left part of Figure 9 and the top panel of Figure 10. We note, however, that the n_H-values corresponding to these contours, $(2.4 \pm 0.2) \times 10^{20}$ and $(2.9 \pm 0.2) \times 10^{20}$ cm^{-2} for the TS+TH+PL and BB+PL models, respectively, significantly exceed the $n_H \simeq (1.1 \pm 0.2) \times 10^{20}$ cm^{-2} obtained from the *ROSAT* PSPC observations (Halpern & Wang 1997), which indicates a discrepancy between the PSPC and EPIC responses at low energies. If we fix n_H at the best-fit PSPC value, the confidence contours shift to higher temperatures and lower radii (see the lower-right EPIC pn contours in Fig. 9), overlapping the FUV contours. For this n_H, the FUV fluxes lie on the extrapolation of the best-fit X-ray TS component at $E(B-V) \lesssim 0.04$ (see Fig. 10, *bottom panel*). Since neither EPIC nor PSPC have been accurately calibrated for very soft spectra, systematic errors can substantially exceed the statistical errors, and the model parameters inferred from such fits may not be very accurate. Therefore, there still remains some uncertainty in the comparison of the X-ray (Wien) and UV (Rayleigh-Jeans) tails of the thermal spectrum. However, even accounting for this uncertainty, Geminga exhibits a fainter UV-optical thermal radiation, relative to the soft X-ray radiation, than the other neutron stars for which such a comparison is possible (see § 4.1).

Figure 10 also shows that the continuation of the best-fit X-ray PL into the optical very strongly overpredicts the observed NIR-optical fluxes for the BB+PL model. However, the predicted and observed fluxes become marginally consistent if we use the PL component inferred from the $E > 2.5$ keV spectral tail.

3.2. *X-Ray Pulsations*

To study the X-ray pulsations of Geminga, we use the same EPIC pn data ($T_{span} = 101.9$ ks, epoch of the middle of the time span 52,369.2997 MJD). First, we measured the pulsation frequency using the Z_n^2 and odds-ratio methods for various energy bands and extraction radii and found most probable frequencies in the range of 4,217,607.75–4,217,607.96 μHz, with typical uncertainties of about 0.1 μHz for individual measurements. For example, the odds-ratio method applied for 42,170 events in the 0.23–4.0 keV band, extracted from a 40″ radius circle, gives $f = 4,217,607.85 \pm 0.10$ μHz for the mean frequency and standard deviation and $f = 4,217,607.86$ (−0.05, +0.05; −0.16, +0.12; −0.24, +0.19) μHz for the median frequency and 68%, 90%, and 99% uncertainties. The most probable frequencies are consistently lower, by 0.1–0.3 μHz, than the frequency $f_{J02} = 4,217,608.0664 \pm 0.0013$ μHz predicted by the J02 ephemeris. However, since the differences do not exceed 3 σ uncertainties of our measurements, it is still possible that the J02 ephemeris is applicable at the epoch of the *XMM-Newton* observation.

We have also directly checked the phase alignment of the light curves extracted from the *XMM-Newton* data with those observed by *ASCA* in 1999 October 5–11. The bottom panel of Figure 11 shows the *XMM-Newton* light curve folded with the J02 ephemeris in the energy band 0.5–2 keV (10,264 counts in a 40″ radius aperture). The top panel of the same figure shows the light curve obtained with the two *ASCA* Gas Imaging Spectrometer (GIS) instruments ($T_{exp} = 207.8$ ks, $T_{span} = 486.5$ ks, epoch of the middle of the time span MJD 51,459.7356; 1819 counts in a 3′ radius aperture) folded with the same ephemeris and in the same energy range. We see that not only are the shapes of these light curves virtually the same, but also their phases are

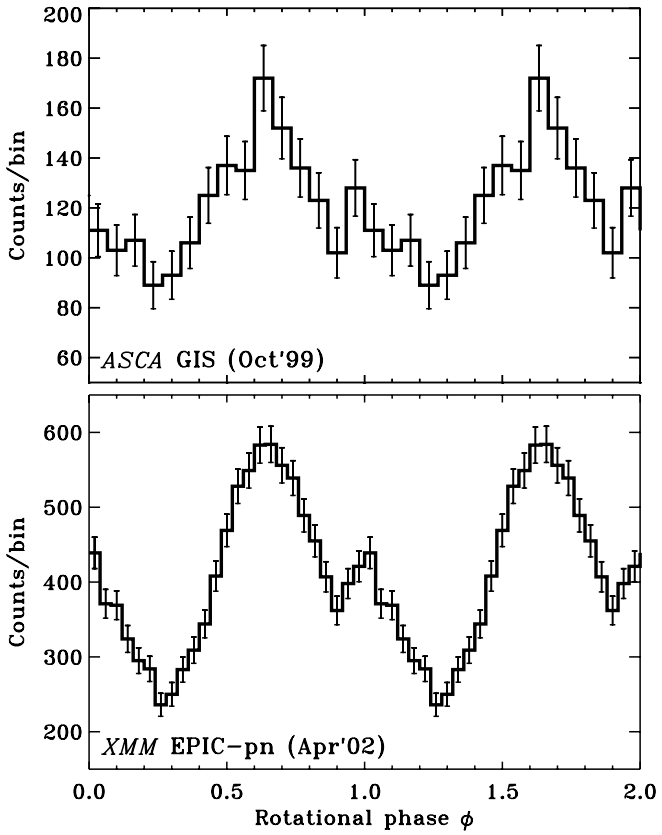

FIG. 11.—*ASCA* GIS and *XMM-Newton* EPIC pn light curves in the 0.5–2 keV range folded with the J02 ephemeris.

in excellent agreement, within the phase uncertainty ($\simeq$0.12) of the J02 timing solution propagated to the epoch of the *XMM-Newton* observation. Therefore, we assume that the J02 ephemeris is still applicable in 2002 April and use it to compare the light curves observed with different instruments.

The background-subtracted light curves in the energy ranges 0.2–0.5, 0.6–1.0, and 2–8 keV are shown in Figure 12. In the 0.2–0.5 and 2–8 keV bands the radiation is dominated by the TS and PL components, respectively, while the 0.6–1.0 keV band was chosen around the maximum of the TH component (see Fig. 10). The light curves were extracted from a smaller, 30″ radius, aperture and a shorter, 80.0 ks, time span (excluding intervals of strong background flares at the beginning and end of the observation) to reduce the background contamination and maximize the S/N. The 2–8 keV light curve (pulsed fraction $f_p = 34\% \pm 8\%$) shows two pronounced peaks per period, resembling the γ-ray light curve (albeit with smaller distance between the peaks) and a hint of a third peak at $\phi \approx 0.2$. On the contrary, the 0.2–0.5 keV light curve ($f_p = 30\% \pm 2\%$) is characterized by one broad peak per period (with small "ripples," perhaps due to contribution from the PL and TH components). The 0.6–1.0 keV light curve shows the highest pulsed fraction, $f_p = 62\% \pm 5\%$, with one asymmetric peak, possibly composed of several peaks associated with contributions from different components in this band (Fig. 10). The minimum of the 0.2–0.5 keV light curve is approximately aligned in phase with one of the minima of the 2–8 keV light curve, being shifted by $\Delta\phi \approx 0.1$ from the sharp dips of the NUV and FUV light curves. (One should remember, however, that the shift can be caused by errors in phase alignment.) Examples of X-ray light curves for other energy ranges can be found in Zavlin & Pavlov

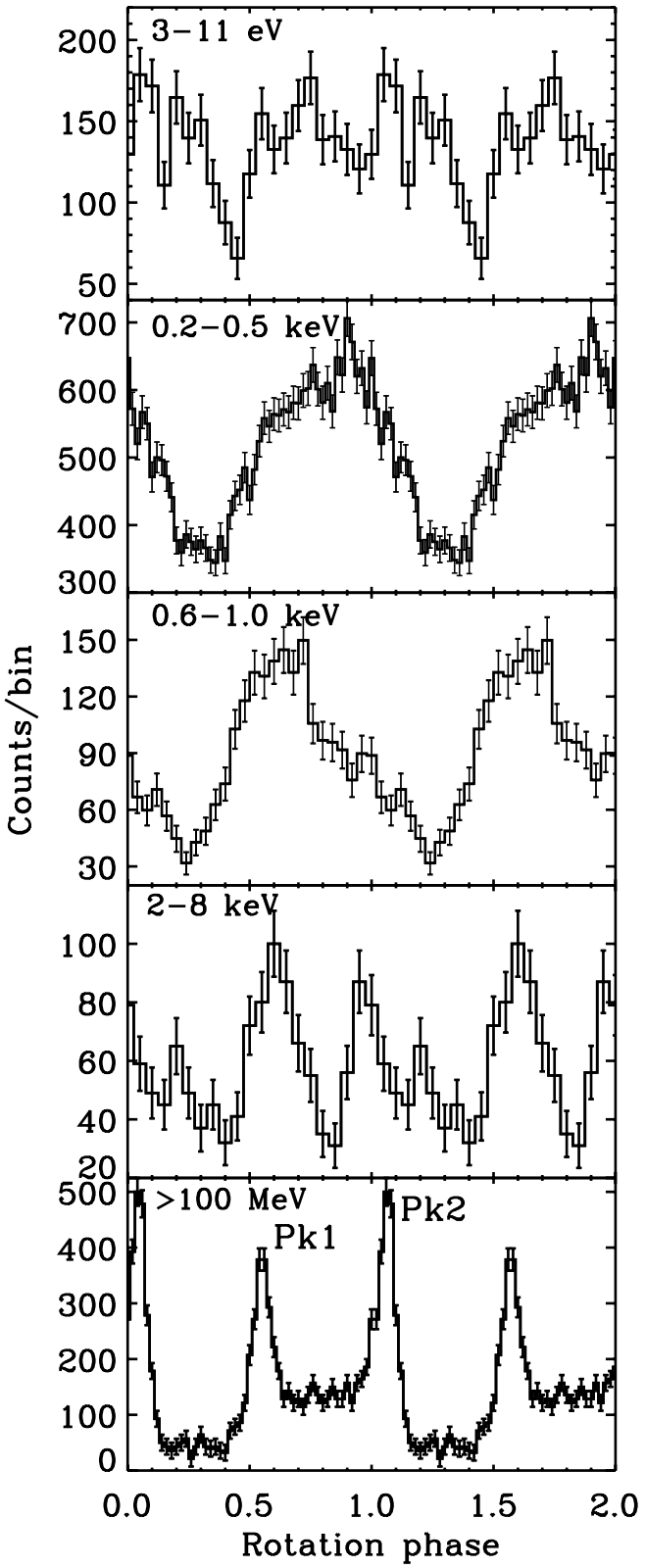

FIG. 12.—Background-subtracted light curves of Geminga in UV (NUV-MAMA + FUV-MAMA), X-ray (EPIC pn), and γ-ray (EGRET) bands, folded with the J02 ephemeris. The γ-ray light curve is taken from J02.

(2004b)[11] and Caraveo et al. (2004a, 2004b). A more detailed discussion of the thermal and nonthermal light curves is presented in § 4.

4. DISCUSSION

The above-described results of the observations of Geminga show that both the NIR-optical-UV and X-ray emission are composed of thermal and nonthermal components, with quite different spectra and light curves. In the following, we discuss the multiwavelength properties of these components separately.

4.1. *Thermal Component(s) of Geminga's Emission*

4.1.1. *Spectrum*

It follows from § 2.2 and § 3.1 that Geminga's radiation is predominantly thermal at 4 eV $\lesssim E \lesssim$ 0.5 keV. The observed FUV and soft X-ray (TS component) spectra represent the Rayleigh-Jeans and Wien tails of the thermal spectrum emitted from the NS surface. The blackbody fits of the soft X-ray emission give the NS surface temperature in a range of 0.45–0.53 MK (≈39–46 eV), corresponding to effective radii of 21–8 km, at $d = 200$ pc (see Figs. 9 and 10). The uncertainty in these parameters is mostly due to the poorly calibrated responses of the EPIC detectors at low energies. Moreover, these temperatures are somewhat lower, and the radii larger, than those estimated from the previous *ROSAT* and *EUVE* observations (Halpern et al. 1996; Halpern & Wang 1997). Since significant variations of the NS temperature and emitting area in a 10 yr span of these observations can hardly be expected, the discrepancy is most likely due to discrepant instrument responses at low energies.

As we have shown in § 3.1, the observed thermal UV spectrum of Geminga either matches the continuation of the thermal X-ray spectrum or lies somewhat below that continuation (up to about 1 stellar magnitude), depending on assumed extinction and X-ray spectral model. On the contrary, other NSs observed in both UV and optical show relatively brighter Rayleigh-Jeans components, well above the continuation of the X-ray thermal spectrum. To demonstrate this difference and show that it is not associated with uncertainties in instrument responses, we reanalyzed the FUV-MAMA and EPIC data on the best-studied isolated neutron star, RX J1856.5−3754 (hereafter J1856 ; see Trümper et al. [2004] for a recent review of its properties). We used the FUV-MAMA observation of 2002 October 26 (exposure time 13,451 s), analyzed the data as described in § 2.2, and confirmed that the spectrum follows a Rayleigh-Jeans law (Pons et al. 2002), with a total flux $F = (1.89 \pm 0.09) \times 10^{-14}$ ergs s^{-1} cm^{-2} in the 1155–1702 Å range. Fitting the FUV-MAMA spectrum with a blackbody model gives $T = (0.45 \pm 0.02) R_{13}^{-2} d_{120}^2$ and $(0.55 \pm 0.02) R_{13}^{-2} d_{120}^2$ MK, at plausible color indices $E(B-V) = 0.01$ and 0.03 ($R_{13} = R/13$ km, $d_{120} = d/120$ pc). The temperature-radius confidence contours of these fits are shown in Figure 13. We also reanalyzed the archival *XMM-Newton* observation of 2002 April 8–9 together with the recent observation of 2004 April 17–18. In the observations of 2002 and 2004, the EPIC pn was operated in small window mode with thin filter (40.0 ks effective exposure) and timing mode with thin filter (64.1 ks effective exposure), respectively. The EPIC MOS observations of 2004 were carried out in full frame mode with thin filter (the same 65.3 ks effective exposures for MOS1 and MOS2). We did not use the EPIC MOS observations of 2002 because MOS1 was operated in timing mode, which is very poorly calibrated for this instrument, and MOS2 was operated in small window mode, with a field of view $100'' \times 100''$ (for the central CCD) too small to reliably subtract the background. We found that the two EPIC pn spectra of J1856 are quite consistent with each other in the 0.3–1 keV range (there is no spectral information available below 0.3 keV in the data collected in timing mode). Since J1856 does not show a nonthermal component, we fit the spectra with a single-component BB model and plot the corresponding confidence contours in Figure 13 ($n_{\rm H,20} = 0.66 \pm 0.3$, $0.04^{+0.12}_{-0.04}$, and $0.03^{+0.41}_{-0.02}$ for the pn, MOS1, and MOS2 detectors, respectively). In the same figure we also plot the confidence contours obtained from fitting the 449.9 ks observation of 2001 October 8–15 with the Low Energy Transmission Grating Spectrometer (LETGS) on *Chandra* (see Burwitz et al. 2003); the corresponding hydrogen column density is $n_{\rm H,20} = 0.86 \pm 0.15$. We see that the observations with different X-ray instruments yield quite different spectral parameters. This demonstrates once more the lack of proper cross-calibration of instrument responses to soft spectra and the fact that systematic uncertainties greatly exceed statistical ones for spectra with good statistics.

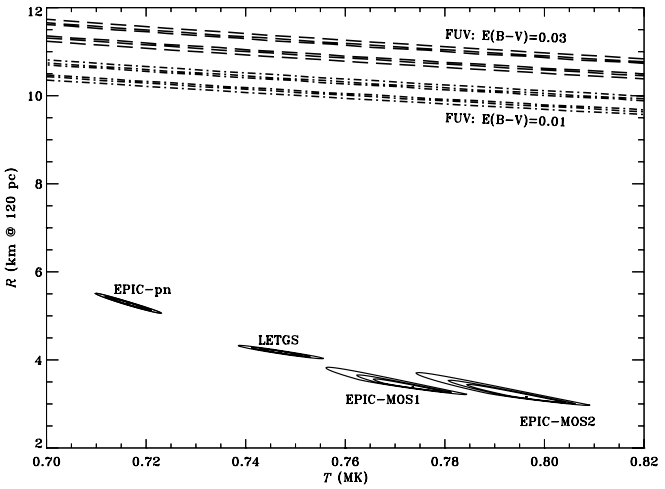

FIG. 13.—Temperature-radius confidence contours (68%, 90%, and 99%) for the isolated neutron star RX J1856.5−3754 obtained from the X-ray observations with different instruments (*solid contours*) and FUV-MAMA observations (*dashed and dash-dotted lines*).

Even with allowance for the uncertainties in instrument responses, we see from Figure 13 that the UV contours lie well above the X-ray contours; i.e., the extrapolation of the X-ray blackbody spectrum of J1856 into the UV-optical range strongly *underpredicts* the observed UV-optical fluxes, contrary to Geminga (cf. Fig. 9). The UV-optical excess in the thermal spectra of J1856 and other so-called X-ray–dim isolated NSs (e.g., RX J0720.4−3125) could be explained assuming that X-rays are emitted from a small hotter area while the optical-UV radiation is emitted from the bulk of NS surface, including colder areas invisible in X-rays (e.g., Pavlov et al. 2002). Obviously, the apparently smaller UV-emitting area of Geminga, as compared to the X-ray–emitting area, cannot be explained by a nonuniform temperature distribution. We might speculate that the temperature distribution over the bulk of Geminga's surface is more uniform than in the case of J1856, e.g., because of a different geometry and strength of the magnetic field that affects the heat conductivity and, hence, the

[11] The inaccurate estimates of pulsed fractions given in Fig. 8 of Zavlin & Pavlov (2004b) should be disregarded.

surface temperature distribution. However, to explain why the more uniformly heated Geminga exhibits quite substantial pulsations of its thermal radiation ($f_p \approx 30\%$ in soft X-rays) while no pulsations have been detected from J1856, one has to assume a special orientation of the spin axis of J1856.

Any realistic interpretation of thermal emission from NSs should take into account possible deviations of thermal spectra emitted from NS surface layers (e.g., atmospheres) from the idealized Planck spectra as well as the anisotropy of the surface emission associated with strong magnetic fields (e.g., Pavlov et al. 1995; Rajagopal et al. 1997; Zavlin & Pavlov 2002). For instance, since the X-ray spectrum emitted from a strongly ionized hydrogen atmosphere is harder than the Planck spectrum, a blackbody fit of such a spectrum gives a temperature exceeding the actual effective temperature by a factor of 1.5–2.5 and a radius a factor of 3–15 smaller than the actual radius of the NS at a given distance. Moreover, the optical part of the spectrum emitted from such an atmosphere strongly exceeds the extrapolation of the blackbody fit of its X-ray spectrum into the optical domain (Pavlov et al. 1996). Although the fully ionized atmosphere models are not applicable to cold NSs (e.g., they give an improbably large radius-to-distance ratio, $R \sim 100$ km at $d = 200$ pc, for Geminga; Meyer et al. 1994), atmospheric effects might, in principle, explain the large difference between the observed UV spectrum and the continuation of the blackbody fit of the X-ray thermal spectrum in J1856 and similar NSs. However, no realistic models adequately describing the observed broadband spectrum of J1856 have been suggested so far, which is not surprising, given the extremely complicated physics of the dense, strongly magnetized matter at the relatively low temperature of the surface layers. If we adopt such an interpretation of the strong deviation of the J1856 broadband spectrum from a pure blackbody spectrum, then we have to explain why the broadband spectrum of Geminga is so different from that of J1856. Possible hypotheses might involve different chemical compositions of the surface layers and/or substantially different magnetic fields (a crude estimate of Geminga's magnetic field is $\sim 2 \times 10^{12}$ G, but the magnetic field of J1856 is quite uncertain[12]). Moreover, the surface layers of Geminga and J1856 might be in different phase states. For instance, one could speculate that the cold surface of Geminga is in a solid state while the (hotter) surface of J1856 is in a gaseous or liquid state, which might explain their different spectra. To distinguish between these possibilities, reliable models for NS thermal emission at relatively low temperatures, accounting for the contribution of molecules in the opacity of gaseous atmospheres with strong magnetic fields (Turbiner & López Vieyra 2004) and possible condensation of the surface layers into a liquid or solid state (van Adelsberg et al. 2004), are to be developed and compared with the observational data. Until reliable models are available, the temperatures and radii obtained from applying simplified models (blackbody, fully ionized atmospheres, partially ionized atmospheres without molecules) should be considered as crude estimates only, and any conclusions based on such fits should be considered with caution. However, although we cannot trust absolute values of the parameters obtained with the aid of simplified models, some interesting qualitative results can be obtained from comparison of the same parameter measured for different NSs. For instance, fits of the soft X-ray spectra of Geminga and an older pulsar B1055−52 with any model available give a lower temperature for the younger Geminga, which may have very interesting implications for the NS cooling models, suggesting different masses of these NSs (Yakovlev & Pethick 2004).

As we mentioned in § 3.1, in addition to the thermal soft (TS) component, the X-ray spectrum of Geminga apparently has a thermal hard (TH) component, with a much higher temperature $T_h \approx 2$ MK and an apparent (isotropic) luminosity $L_h \sim 4 \times 10^{29}$ ergs s^{-1}. Although such a component has been seen in the spectra of other middle-aged pulsars, the effective radius, $R_h \sim 50 d_{200}$ m, for Geminga's TH component is surprisingly small in comparison with the conventional polar cap radius, $R_{\rm pc} = (2\pi f R^3)^{1/2} c^{-1/2} \approx 300$ m, suggested by the pulsar models. Such a small value of R_h might be explained by a projection effect (if the magnetic axis remains almost perpendicular to the line of sight in the course of NS rotation), but this explanation can hardly be reconciled with the high pulsed fraction at energies where the TH component contribution is maximal (see § 4.1.2). On the other hand, we should remember that the TS component was obtained assuming Planck spectra for both thermal components and a single power law for the magnetospheric spectrum. Because both these assumptions are not necessarily correct, we cannot rule out the possibility that the "TH component" is simply associated with a harder, high-energy tail of the surface radiation (compared to the pure Wien spectrum) or that it is due to a steepening of the slope of the phase-integrated magnetospheric spectrum with decreasing photon energy (see § 4.2).

4.1.2. *Pulsations in Thermal Emission*

One of the most intriguing results of our STIS MAMA observations of Geminga is the strong, nonsinusoidal pulsations in the FUV range, where the spectrum is dominated by the thermal component, most likely emitted from the bulk of NS surface. The shape of the FUV pulsations is different from that of the soft X-ray pulsations, where the TS component dominates (see Fig. 12). Obviously, neither FUV nor soft X-ray pulsations can be produced by the locally isotropic blackbody emission. To explain the unusual pulse shape and the large pulsed fraction of the thermal FUV and soft X-ray radiation, we have to invoke effects of strong magnetic field on the angular dependence of NS surface emission or assume that there is a "screen" in the NS magnetosphere that may partially eclipse the surface emission at some rotation phases.

In a strong magnetic field, $B \gg 10^{11}(E/1\ \text{keV})$ G, when the electron cyclotron energy E_c exceeds the photon energy, the local emission is essentially anisotropic (in particular, beamed along the direction of the magnetic field), which may lead to strong pulsations of the thermal radiation. The angular distribution and the shape of pulsations depend on the properties of the emitting region. For instance, the angular distribution of local emission from a fully ionized NS atmosphere shows a strong, narrow peak [$\Delta\theta \sim (E/E_c)^{1/2}$] along the magnetic field (pencil component) and a broad fanlike component across the magnetic field (Pavlov et al. 1994). When integrated over the visible surface of a NS with a dipole magnetic field, the angular distribution of NS radiation is beamed along the magnetic axis, even in the case of a uniformly heated NS surface (Zavlin & Pavlov 2002). Such peaks could explain the soft X-ray pulsations (at $E \gtrsim kT_{\rm eff}$), including the observed increase of pulsed fraction with energy. In this hypothesis, the 0.2–0.5 keV pulse profile (see Fig. 12) can be interpreted as a sum of a smooth thermal component (the broad thermal peak, with a maximum at $\phi \approx 0.8$, corresponds to the closest approach of the magnetic axis to the line of sight), and small "wiggles" (e.g., at $\phi \approx 0.9$)

[12] For instance, Pavlov & Zavlin (2003) consider the possibility that J1856 is a millisecond pulsar with a very low magnetic field, $B \sim 10^8$–10^9 G, while Trümper et al. (2004) suggest that it has a very strong field $B > 10^{13}$ G.

due to the contribution of the magnetospheric radiation. However, at $E \ll kT_{\rm eff}$ the peaks in the model angular distribution are too low to be responsible for the observed FUV pulsations. On the other hand, as we mentioned above, the fully ionized atmosphere models are not directly applicable to the cold Geminga, while the partially ionized atmospheres have not been well investigated.

If the NS surface matter is in a condensed state, we also should expect an anisotropic emission. Although the angular distribution of emission from a condensed surface has not been studied, the examples of spectral emissivity for several directions, calculated by van Adelsberg et al. (2004), suggest that at least local radiation is beamed along the magnetic field. To understand whether the radiation from the entire NS surface can show pulsations similar to those observed from Geminga, the local specific fluxes should be integrated over the visible NS surface for various magnetic field geometries and orientations of the spin and magnetic axes (see Pérez-Azorín et al. 2005 for a few examples).

An alternative explanation for the narrow deep minima in the UV pulse profiles could be a partial eclipse by an object corotating with the NS. Since the shapes of the UV and soft X-ray light curves are different (in particular, the minima are broader in soft X-rays), the eclipsing object should have a wavelength-dependent effective size. A natural candidate for such a screen is the magnetospheric electron-positron plasma, which can absorb the NS surface radiation as a result of the cyclotron resonance scattering in a resonance layer, where the cyclotron energy is equal to the photon energy in the rest frame of the electron (e.g., Blandford & Scharlemann 1976). Two types of models have been discussed for the scattering region: a stationary nonrelativistic plasma in the closed magnetic field lines zone (Rajagopal & Romani 1997; Wang et al. 1998; Ruderman 2003) and streams of ultrarelativistic electron-positron pairs ejected along the open field lines (e.g., Lyubarskii & Petrova 1998, 2000, and references therein). In the latter case, the effects of the resonant inverse Compton scattering on the properties of observed UV and/or X-ray radiation have not been investigated in detail; however, crude estimates show that an extremely large pair multiplicity is needed to reach an optical thickness of $\gtrsim 1$. In the case of nonrelativistic plasma in the closed zone, which can be supported against the gravitational force by the thermal radiation pressure enhanced by the cyclotron resonance (Mitrofanov & Pavlov 1982; Rajagopal & Romani 1997), the effects of resonant cyclotron scattering become significant if the electron/positron number density is a factor of $\sim 10^2$ larger than the corotation (Goldreich-Julian) density, $n_{\rm GJ} \sim 10^{13}$ cm^{-3} for Geminga. The electron-positron pairs could be supplied from acceleration zones, but rapid pair production (large multiplicity) is needed to provide such high densities. In addition, it remains unclear how the electrons/positrons would lose the longitudinal momentum to become nonrelativistic particles (the transverse momentum is essentially nonrelativistic because of the fast synchrotron/cyclotron losses). If, nevertheless, there is such a nonrelativistic plasma screen in the closed zone, the wavelength dependence of its optical thickness depends on spatial distribution of scattering particles. In particular, the assumption that the minima in the UV light curves of Geminga are caused by such a rotating screen implies a significant amount of electron-positron pairs at a distance of $\sim 15R_{\rm NS}$, where the magnetic field is $\sim 10^9$ G. One might speculate that the broader minima in the soft X-ray light curve are also caused by a partial eclipse by the screen. In this case, the X-ray resonance layer (at a distance $\sim 5R_{\rm NS}$) should subtend a larger solid angle than the UV resonance layer. Alternatively, if the soft X-ray pulsations are caused not by the screen but by the intrinsic anisotropy of the thermal radiation in the strong magnetic field (see above), then the magnetosphere is transparent for the X-rays we observe, i.e., the inner boundary of the plasma screen is located beyond $\sim 5R_{\rm NS}$.

To infer the size of the putative screen and understand the spatial distribution of electrons and positrons, independent information on the orientation of the spin and magnetic axes would be very useful. Such information could be obtained from X-ray pulsations of the TH component emitted by hot polar caps, which apparently contribute to the X-ray spectrum around ~ 0.7 keV (see Fig. 10). Caraveo et al. (2004b) have interpreted the EPIC data as displaying a varying TH component arising from a rotating polar cap. However, in our analysis the contribution of this component to the spectral flux is small and is not clearly seen in the pulse profile. Indeed, the 0.6–1.0 keV pulse profile (Fig. 12) can be decomposed into a broad thermal pulse with a maximum at $\phi \approx 0.8$, similar to the mainly thermal 0.2–0.5 keV pulse, and a narrower nonthermal pulse centered at the same phase, $\phi \approx 0.6$, as the higher of the two purely nonthermal peaks in 2–8 keV light curve. In other words, we see no convincing evidence for the TH component (hence, polar caps) in the energy-dependent light curves. More definitive information on the axis orientation could be obtained from phase-resolved X-ray polarimetry (e.g., Pavlov & Zavlin 2000; Lai & Ho 2003), but it is not possible with the currently operating X-ray missions.

4.2. *Nonthermal Emission*

The multiwavelength observations of Geminga show that its emission in the NIR-optical, hard X-rays, and γ-rays is nonthermal, presumably generated in the NS magnetosphere. The comparative analysis of the results of these observations provides an opportunity to understand the mechanisms responsible for the magnetospheric emission in different energy bands.

First, we can compare the phase-integrated X-ray spectra at $E \gtrsim 2$ keV and optical spectra at $E \lesssim 3$ eV, where the nonthermal emission dominates. As shown in § 3.1, the fits to the X-ray spectrum yield substantially different slopes of the PL component, depending on whether the TH component is included in the model. With the data available, we cannot statistically prove or reject the TH component. However, we can extrapolate the PL components of the two different models (with and without the TH component) to the optical and compare the extrapolations with the observed nonthermal spectra (Figs. 7 and 10). The PL fit of the 2.5–10 keV tail has about the same slope as the optical PL component [$\Gamma_{\rm X} = 1.56 \pm 0.24$, $\Gamma_O = 1.46 \pm 0.12$ and 1.41 ± 0.13 for $E(B-V) = 0.03$ and 0.07, respectively], and the extrapolation of the X-ray PL spectrum is marginally consistent with the optical fluxes (the uncertainty of the extrapolation is shown in Fig. 10 [*bottom panel*] and Fig. 14 for absorbed and unabsorbed spectra, respectively). The NIR through X-ray spectrum can be crudely described by a PL model with a slope $\Gamma_{\rm OX} \approx 1.3$, which is smaller than $\Gamma_{\rm X}$ and Γ_O, but the differences are close to 1 σ uncertainties of the photon indices. Similar NIR through X-ray behavior, with $\Gamma_{\rm X} \approx \Gamma_O \approx 1.5$, has been seen in another middle-aged pulsar, B0656+14 (Pavlov et al. 2002; Zavlin & Pavlov 2004b). Such behavior implies that the optical and X-ray emission are generated by the same population of relativistic particles with a PL energy spectrum and by the same (likely synchrotron) mechanism. This conclusion is supported by the fact that the ratio of optical-to–X-ray luminosities is about the same for all the pulsars observed in both X-rays and optical, despite a large scatter of the X-ray and optical "efficiencies," $L_{\rm X}/\dot{E}$ and $L_O/\dot{E}$ (Zavlin & Pavlov 2004a).

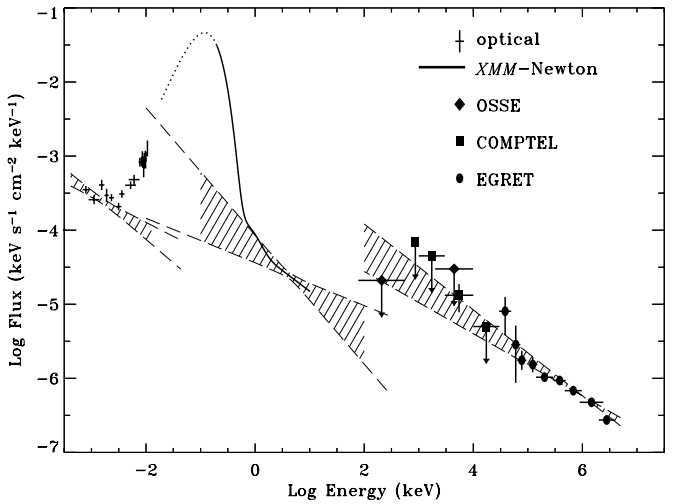

FIG. 14.—Multiwavelength phase-integrated spectrum of Geminga. The EGRET, COMPTEL, and OSSE points are from Mayer-Hasselwander et al. (1994), Kuiper et al. (1996), and Strickman et al. (1996), respectively. Fits with the PL model for three spectral bands (with ± 1 σ uncertainties) and their extrapolations are shown.

If the TH component is not included in the fit, the extrapolation of the PL component ($\Gamma_X = 2.02 \pm 0.05$) of the BB+PL fit of the 0.2–10 keV spectrum exceeds the optical fluxes by more than 2 orders of magnitude (see Fig. 10, *top panel*). This might imply a flattening of the spectrum with decreasing energy, as observed in the younger Crab and Vela pulsars (Sollerman et al. 2000; Romani et al. 2005). However, the continuation toward higher energies of the NIR-optical PL component crosses the X-ray PL component at energies $\gtrsim$10 keV, which means a "double break" of the spectrum between the optical and X-ray bands (i.e., Γ becomes smaller than Γ_O and then increases to Γ_X). Although such behavior has been suggested (with a considerable uncertainty) for the young LMC pulsar B0540−69 (Serafimovich et al. 2004), it was not observed in other pulsars and currently does not look very plausible.

One can also extrapolate the best-fit X-ray PL components toward higher energies to compare with the γ-ray data (Fig. 14). The *CGRO* EGRET γ-ray spectrum has a slope $\Gamma_\gamma = 1.50 \pm 0.08$ in the energy range 70 MeV to 2 GeV (Mayer-Hasselwander et al. 1994), close to that inferred from the PL fit of the 2.5–10 keV tail. However, the extrapolation of the EGRET spectrum into the X-ray range exceeds the X-ray PL tail by about 1 order of magnitude, while the extrapolation of the X-ray spectrum into the EGRET range underpredicts the observed flux by a factor of $\sim$20 at 2 GeV. (The discrepancy is of course much larger if we take the PL component of the BB+PL fit.) Interestingly, the extrapolation of the PL that crudely connects the optical and X-ray points ($\Gamma_{OX} \approx 1.3$) predicts approximately correct γ-ray fluxes at $\sim$0.5 GeV, but the difference in the slopes is a factor of 2.5 larger than the 1 σ error of Γ_γ. Thus, unless there is a significant systematic error in the EGRET data analysis,[13] we have to conclude that there should be a double break in the spectrum between the EPIC and EGRET bands, which likely means that the γ-ray emission is generated by a different mechanism (e.g., curvature radiation), or by a different population of relativistic particles, than the optical and X-ray emission. The *CGRO* COMPTEL and OSSE observations were not sensitive enough to prove or reject the existence of such a break (Kuiper et al. 1996; Strickman et al. 1996).

In the above discussion on the connection between the NIR-optical and hard X-ray phase-integrated spectra, it was assumed that each of them could be adequately described by a PL model. In fact, it is quite plausible that the nonthermal high-energy radiation of pulsars is composed of several components that are peaked in different directions (phases) and have different spectral slopes, as it has been recently observed in the hard X-ray emission of the Vela pulsar (Harding et al. 2002) and is routinely seen in the γ-ray range (e.g., Fierro et al. 1998). In this case one should expect the phase-integrated spectrum to have a concave shape (in a log-log scale), with excesses at low and high energies dominated by the softer and harder components, respectively. Some indications of such a concave spectrum are seen in Geminga's nonthermal X-ray component: while fitting the high-energy tail of Geminga's EPIC pn spectrum with a single PL and different low-energy cutoffs ($E_{\rm min}$), we noticed that the best-fit Γ increases with decreasing $E_{\rm min}$ (e.g., $\Gamma = 1.45 \pm 0.30$, 1.56 ± 0.24, and 1.60 ± 0.20 at $E_{\rm min} = 3.0$, 2.5, and 2.0 keV, respectively). Although the change of Γ is not statistically significant, such a trend suggests that the tail is concave rather than flat, which, in turn, hints that there may be several emission components (unless the high-energy tail of the thermal component is harder than in the thermal models we used). Unfortunately, the S/N at $E \gtrsim 2$ keV is too low to verify this directly with phase-resolved spectroscopy.

It is also interesting to compare the nonthermal pulsations in different energy bands. The γ-ray light curve (Fig. 12, *bottom panel*) shows two peaks per period, at $\phi \simeq 0.55$ (peak 1) and $\phi \simeq 1.05$ (peak 2), with a bridge between them. In the X-ray 2–8 keV band, we also see two peaks, but they are broader, their separation ($\Delta\phi \approx 0.35$ or 0.65) differs significantly from the $\Delta\phi \simeq 0.5$ in γ-rays, and about 60%–70% of the 2–8 keV emission is unpulsed, in contrast to about 100% pulsed γ-ray emission. We cannot determine from these data alone what is the correspondence (if any) between the X-ray and γ-ray peaks (e.g., the higher X-ray peak could correspond to either peak 2 or peak 1, which would mean that it trails the corresponding γ-ray peak by $\delta\phi \approx 0.55$ or 0.05, respectively). It is tempting to identify the stronger X-ray emission at phases $\sim$0.1–0.5 as a bridge similar to that in the γ-ray light curve (which would mean that the higher X-ray peak corresponds to peak 2), but the low S/N at these phases makes this identification rather uncertain. Moreover, since no statistically significant change of the peak phases with energy is seen in the 0.03–3 GeV EGRET range, it is quite possible that the 2–8 keV X-ray peaks do not directly correspond to the γ-ray peaks, being produced by a distinct mechanism. Observations at intermediate energies, 10 keV to 10 MeV, are needed to clarify this issue.

As we mentioned above, the highly asymmetric pulse profile at intermediate X-ray energies 0.6–1 keV can possibly be decomposed into two components: a broad, likely thermal, component centered at $\phi \approx 0.75$, similar to that seen in the 0.2–0.5 keV band, and a narrower nonthermal peak around the phase $\phi \approx 0.6$ of the higher of two 2–8 keV peaks. However, the putative nonthermal peak at 0.6–1 keV looks significantly broader than the corresponding peak at 2–8 keV, while the lower 2–8 keV peak is hardly seen in the 0.6–1 keV band. The

[13] We should note in this respect that Grenier et al. (1993) reported a substantially softer spectrum from the *COS B* observations of Geminga: $\Gamma_\gamma = 1.84 \pm 0.05$ in the 0.05–5 GeV range, or 2.02 ± 0.07 in the 0.14–5 GeV range, with an indication of a spectral turnover below $\sim$0.2 GeV. With such a soft γ-ray spectrum, a double spectral break in between the EPIC and EGRET bands is certainly required. On the other hand, Fierro et al. (1998) found a somewhat harder spectrum from the EGRET data: $\Gamma_\gamma = 1.42 \pm 0.02$ in the 0.03–2 Gev range. Given the large uncertainties in Γ_X (including systematic ones; see the discussion in the next paragraph), the necessity of the double break becomes less certain.

0.2–0.5 keV light curve is clearly dominated by the very broad, thermal peak centered at $\phi \approx 0.8$; in the simple dipole geometry of the magnetic field (and the corresponding axisymmetric temperature distribution), this phase corresponds to the nearest approach of the only visible magnetic pole to the center of stellar disk. Small contributions from the nonthermal radiation are likely seen even at these low energies; e.g., some excess emission over the smooth pulse profile at $\phi \approx 0.55$–0.65 might be due to the nonthermal peak centered at $\phi = 0.6$, while the narrow "subpeak" at $\phi \approx 0.9$ might be associated with the lower of two 2–8 keV peaks. So it seems that the two nonthermal X-ray peaks persist through the whole observed X-ray range, being most clearly seen in the 2–8 keV band, where they are not "contaminated" by the thermal radiation.

The connection between the optical-UV and X-ray–γ-ray pulsations (see Figs. 8 and 12) remains unclear. We do see two peaks in the FUV band, with about 0.45 phase separation, but they may not be related to the hard X-ray and/or γ-ray pulsations because the FUV spectrum is mostly thermal. We see only one broad peak in the NUV light curve, where the nonthermal contribution is substantial, $\sim$30%–40%, but we cannot rule out the possibility that it is composed of two peaks because the NUV light curve is very noisy. Two peaks with a separation of about 0.5 in phase, similar to the γ-ray peaks, were apparently seen in the optical *B* band (Shearer et al. 1998), but those observations were compromised by a very high variable background.

It is interesting to compare the multiwavelength nonthermal radiation of Geminga with theoretical models. For instance, the outer gap model by Zhang & Cheng (2001) predicts one nonthermal X-ray peak coinciding in phase with the γ-ray peak 1 and one soft thermal X-ray peak centered at the phase of the γ-ray peak 2. However, we see two nonthermal X-ray peaks, while the presumably thermal X-ray peak is centered in the middle between peak 1 and peak 2. The latter property is expected in the polar cap models for high-energy radiation, which assume that both nonthermal X-rays and γ-rays are emitted along a hollow cone inscribed in the surface formed by the last open field lines (Harding & Muslimov 1998). In this model, the two nonthermal peaks are seen at the phases when the line of sight is tangent to the cone at the site where the radiation is generated (a few NS radii from the surface), which implies that only one pole is visible (i.e., the angles between the rotation and magnetic axes and rotation axis and line of sight are $\lesssim 30^\circ$). The different separation between the X-ray peaks, in comparison with that of the γ-ray peaks, might mean that they are generated at different distances from the NS (e.g., closer to the NS if the highest of the two 2–8 keV peaks corresponds to the γ-ray peak 1), while their larger widths suggest that the X-rays are less beamed than the γ-rays. We might speculate that the two peaks become even broader and closer in the NUV band, so that they appear as one peak, but such a trend is not seen in the optical.

Alternatively, the soft X-ray pulsations may still be magnetospheric in origin. This is, in fact, natural in the outer magnetosphere picture of Romani & Yadigaroglu (1995). In their model the closest polar cap approach is $\delta\phi \sim 0.1$ before the γ-ray peak 1, while the cap producing the observed γ-ray emission passes $\delta\phi = 0.5$ later, at $\phi \approx 0.95$ in Figure 12. These phases are close to the primary and possible secondary UV minima of Figure 8. In the Dyks & Rudak (2003) two-pole model, the γ-ray peaks arise from opposite hemispheres, but the phase of closest pole approach is rather similar. In either case, it seems natural to interpret these minima as the result of scattering screens above the polar caps removing flux (§ 4.1.2). It would be very surprising if the FUV pulse minimum level represented the true Rayleigh-Jeans surface flux (with the broad peaks being hot-cap or nonthermal emission), as this would require a remarkably low NS temperature. In this interpretation there would be a distribution of soft nonthermal components dominating the X-ray pulse, mimicking here the TH component and perturbing the fit of the TS component. Little if any of the pulsed emission would come from a thermal cap. The (unpulsed) X-ray surface emission would be about 30% lower than that fitted for the TS component, allowing better agreement with the Rayleigh-Jeans UV flux in Figure 9. Higher statistics FUV phase-resolved spectra are required to determine whether the closest approach of the magnetic axis to the line of sight is associated with the FUV minima or the soft X-ray maxima.

5. SUMMARY

The results of our work can be summarized as follows.

1. The STIS MAMA observations of Geminga have allowed us to detect, for the first time, its FUV radiation, measure the FUV spectrum and NUV flux, and detect FUV and NUV pulsations. We also measured the flux in the ACS WFC F555W band. To understand the multiwavelength properties of Geminga's radiation, we analyzed its X-ray spectrum and pulsations observed with *XMM-Newton*.

2. The phase-integrated NIR through FUV spectrum consists of two components, thermal and nonthermal. The thermal component, which dominates at $\lambda \lesssim 3000$ Å, is emitted from the NS surface. Its flux corresponds to a brightness temperature $T_{\rm RJ} = (0.3$–$0.4)(d_{200}/R_{13})^2$ MK. The nonthermal component, which is likely generated in the pulsar's magnetosphere, shows a PL spectrum with photon index $\Gamma_O = 1.3$–1.6 and dominates at NIR-optical wavelengths. We do not confirm the previously claimed spectral feature in the *V* band.

3. The phase-integrated X-ray spectrum is dominated by a thermal soft component at $E \lesssim 0.5$ keV, with a blackbody temperature $T_s \approx 0.5$ MK and radius $R_s \approx 13 d_{200}$ km. Extrapolation of this spectrum into the optical-UV domain slightly overpredicts the thermal component of the observed UV spectrum, in contrast to all the other NSs observed in both X-ray and optical-UV ranges. This might be associated with the very low temperature or a different chemical composition of Geminga's surface. Under the assumption that the blackbody model properly describes the thermal spectra while the nonthermal spectrum is a simple power law, an additional thermal component is required to fit the X-ray spectrum, with a higher temperature $T_h \approx 2$ MK and a small size of the emitting region $R_h \approx 50$ m. It is not clear whether this component is real or appears because the simplified model spectra were used in the fits. Indeed, several soft nonthermal components could contribute to the X-ray emission, leaving the residual thermal surface flux in better agreement with the UV Rayleigh-Jeans emission.

4. The slope of the X-ray nonthermal component, which dominates at $E \gtrsim 1$ keV, is not well constrained, $\Gamma_{\rm X} \approx 1.2$–$2.0$, because of a large background at these energies and, possibly, some deviations of the spectrum from a simple PL model. Its extrapolation into the NIR-optical domain is either marginally consistent with the observed fluxes or goes above these fluxes, requiring a flattening of the nonthermal spectrum with decreasing photon energy. Most likely, the optical radiation and the X-rays are emitted by the same population of relativistic particles in Geminga's magnetosphere and generated by the same mechanism. On the other side, the continuations of the nonthermal X-ray and γ-ray spectra do not match smoothly, which suggests different radiation mechanisms in these energy bands.

5. Unexpectedly, we detected strong pulsations in the FUV band. The light curve of the predominantly thermal FUV radiation, with a narrow, deep minimum and possibly another minimum shifted by about half a period, differs significantly from the light curve of the thermal soft X-ray radiation, which shows one broad, smooth peak per period, possibly distorted by a small contribution from the magnetospheric component. Because the FUV pulsations can hardly be explained by an anisotropic temperature and/or magnetic field distributions, we suggest that they could be associated with a resonance scattering of the thermal UV photons in the NS magnetosphere.

6. The light curve of the nonthermal X-ray emission shows two peaks, as the γ-ray light curve does, but the X-ray peaks are substantially broader, and their separation differs significantly from the half-period separation of the γ-ray peaks. At least one of the nonthermal peaks is apparently seen at lower X-ray energies, superimposed on the broader peak of thermal emission. We see no clear connection between the nonthermal X-ray pulsations and single-peaked NUV pulsations. Two peaks have been apparently seen in the optical, but this very noisy light curve is badly in need of confirmation.

To conclude, the *HST* STIS MAMA observations have allowed us to study the UV spectrum and pulsations of Geminga. Combined with the results of the previous optical and γ-ray observations and our analysis of the *XMM-Newton* data, this study has provided a connection between different energy bands for the thermal and magnetospheric components and elucidated the multiwavelength picture of Geminga's radiation. However, some important properties of this radiation remain unclear. First, the true nature of the UV (particularly FUV) pulsations is still uncertain. To understand it, phase-resolved spectroscopy of the FUV radiation would be particularly useful, which would require deeper FUV-MAMA observations, quite feasible with the *HST* STIS if it is brought back to life in a future servicing mission. Second, it remains unclear whether we indeed see a small, high-temperature polar cap or whether this is an artifact caused by the use of simplified spectral models. To answer this question we need realistic models for thermal and nonthermal X-ray radiation and phase-resolved spectroscopy at $E \gtrsim 0.5$ keV with high S/N. Third, we do not understand the connection between the nonthermal X-ray emission and γ-ray emission. This problem could be resolved by observations in a 10 keV to 10 MeV band with a future mission equipped with detectors more sensitive in this energy range than the detectors of the *RXTE* and *INTEGRAL* missions. *NUSTAR*, for example, should be able to offer sensitive measurements in the hard X-ray range.

We thank Rosa Diaz-Miller for the help with the STIS data analysis, Divas Sanwal for useful discussions, Hans-Albert Mayer-Hasselwander for providing the γ-ray data, and Igor Volkov for the help with timing analysis. The work of V. E. Z. is supported by a National Research Council Research Associateship Award at NASA MSFC. Support for programs GO-9182 and GO-9756 was provided by NASA through a grant from the Space Telescope Science Institute, which is operated by the Association of Universities for Research in Astronomy, Inc., under NASA contract NAS5-26555. This work was also partly supported by NASA grants NAG5-10865, NAG5-13344, and NNG 04GI80G.

REFERENCES

Bertch, D. L., et al. 1992, Nature, 357, 306
Bignami, G. F., Caraveo, P. A., & Lamb, R. C. 1983, ApJ, 272, L9
Bignami, G. F., Caraveo, P. A., Mignani, R., Edelstein J., & Bowyer, S. 1996, ApJ, 456, L111
Bignami, G. F., Caraveo, P. A., & Paul, J. A. 1988, A&A, 202, L1
Bignami, G. F., Caraveo, P. A., Paul, J. A., Salotti, L., & Vigroux, L. 1987, ApJ, 319, 358
Blandford, R. D., & Scharlemann, E. T. 1976, MNRAS, 174, 59
Bohlin, R. 1999, Ultraviolet Imaging Telescope Research Activities (Baltimore: STScI)
Brown, T., et al. 2002, in *HST* STIS Data Handbook, ver. 4.0, ed. B. Mobashner (Baltimore: STScI), http://www.stsci.edu/hst/stis/documents/handbooks/currentDHB/STIS_longdhbTOC.html
Buccheri, R., et al. 1983, A&A, 128, 245
Burwitz, V., Haberl, F., Neuhäuser, R., Predehl, P., Trümper, J., & Zavlin, V. E. 2003, A&A, 399, 1109
Caraveo, P. A., Bignami, G. F., De Luca, A., Mereghetti, S., Pellizzoni, A., Mignani, R., Tur, A., & Becker, W. 2003, Science, 301, 1345
Caraveo, P. A., Bignami, G. F., De Luca, A., Pellizzoni, A., Mereghetti, S., Mignani, R. P., Tur, A., & Becker, W. 2004a, Mem. Soc. Astron. Italiana, 75, 470
Caraveo, P. A., Bignami, G. F., Mignani, R., & Taff, L. G. 1996, ApJ, 461, L91
Caraveo, P. A., De Luca, A., Mereghetti, S., Pellizzoni, A., & Bignami, G. F. 2004b, Science, 305, 376
Dyks, J., & Rudak, B. 2003, ApJ, 598, 1201
Fierro, J. M., Michelson, P. F., & Nolan, P. L. 1998, ApJ, 494, 734
Gregory, P. C., & Loredo, T. J. 1996, ApJ, 473, 1059
Grenier, I. A., Hermsen, W., & Henriksen, R. N. 1993, A&A, 269, 209
Halpern, J. P., Grindlay, J. E., & Tytler, D. 1985, ApJ, 296, 190
Halpern, J. P., & Holt, S. S. 1992, Nature, 357, 222
Halpern, J. P., Martin, C., & Marshall, H. L. 1996, ApJ, 473, 37L
Halpern, J. P., & Ruderman, M. 1993, ApJ, 415, 286
Halpern, J. P., & Tytler, D. 1988, ApJ, 330, 201
Halpern, J. P., & Wang, F. Y.-H. 1997, ApJ, 477, 905
Harding, A. K., & Muslimov, A. G. 1998, ApJ, 500, 862
Harding, A. K., Strickman, M. S., Gwinn, C., Dodson, R., Moffet, D., & McCulloch, P. 2002, ApJ, 576, 366
Harlow, J. J. B., Pavlov, G. G., & Halpern, J. P. 1998, BAAS, 30, 1309
Jackson, M. S., Halpern, J. P., Gotthelf, E. V., & Mattox, J. R. 2002, ApJ, 578, 935 (J02)
Kargaltsev, O., Pavlov, G. G., & Romani, R. W. 2004, ApJ, 602, 327
Kaspi, V. M., Roberts, M. S. E., & Harding, A. K. 2006, in Compact Stellar X-Ray Sources, ed. W. H. G. Lewin & M. van der Klis (Cambridge: Cambridge Univ. Press), in press (astro-ph/0402136)
Kim Quijano, J., et al. 2003, STIS Instrument Handbook, ver. 7.0 (Baltimore: STScI), http://www.stsci.edu/hst/stis/documents/handbooks/currentIHB/stis_ihbTOC.html
Komarova, V., et al. 2003, in Pulsars, AXPs, and SGRs Observed with *BeppoSAX* and Other Observatories, ed. G. Cusumano, E. Massaro, & T. Mineo (Rome: Aracne Editrice), 77
Koptsevich, A. B., Pavlov, G. G., Zharikov, S. V., Sokolov, V. V., Shibanov, Yu. A., & Kurt, V. G. 2001, A&A, 370, 1004
Kuiper, L., Hermsen, W., Bennett, K., Connors, A., Much, R., Ryan, J., Schönfelder, V., & Strong, A. 1996, A&AS, 120, 73
Kuz'min, A. D., & Losovskii, B. Ya. 1997, Astron. Lett., 23, 283
Lai, D., & Ho, W. C. G. 2003, ApJ, 588, 962
Landsman, W. 1998, Characteristics of the FUV-MAMA Dark Rate (Baltimore: STScI)
Lyubarskii, Y. E., & Petrova, S. A. 1998, A&A, 337, 433
———. 2000, A&A, 355, 406
Malofeev, V. M., & Malov, O. I. 1997, Nature, 389, 697
Martin, C., Halpern, J. P., & Schiminovich, D. 1998, ApJ, 494, L211
Mayer-Hasselwander, H.-A., et al. 1994, ApJ, 421, 276
McLaughlin, M. A., Cordes, J. M., Hankins, T. H., & Moffett, D. A. 1999, ApJ, 512, 929
Meyer, R. D., Pavlov, G. G., & Mészáros, P. 1994, ApJ, 433, 265
Mignani, R. P., Caraveo, P. A., & Bignami, G. F. 1998, A&A, 332, L37
Mitrofanov, I. G., & Pavlov, G. G. 1982, MNRAS, 200, 1033
Pavlov, G. G., Shibanov, Yu. A., Ventura, J., & Zavlin, V. E. 1994, A&A, 289, 837
Pavlov, G. G., Shibanov, Yu. A., Zavlin, V. E., & Meyer, R. D. 1995, in The Lives of the Neutron Stars, ed. M. A. Alpar, Ü. Kizilolu, & J. van Paradijs (NATO ASI Ser. C, 450; Dordrecht: Kluwer), 71
Pavlov, G. G., & Zavlin, V. E. 2000, ApJ, 529, 1011
———. 2003, in Proc. XXI Texas Symposium on Relativistic Astrophysics, ed. R. Bandiera, R. Maiolino, & F. F. Manucci (Singapore: World Scientific), 319

Pavlov, G. G., Zavlin, V. E., & Sanwal, D. 2002, in Proc. 270 Heraeus Seminar on Neutron Stars, Pulsars, and Supernova Remnants, ed. W. Becker, H. Lesch, & J. Trümper (MPE Rep. 278; Garching: MPE), 273
Pavlov, G. G., Zavlin, V. E., Trümper, J., & Neuhäuser R. 1996, ApJ, 472, L33
Pérez-Azorín, J. F., Miralles, J. A., & Pons, J. A. 2005, A&A, 433, 275
Pons, J. A., Walter, F. M., Lattimer, J. M., Prakash, M., Neuhäuser, R., & An, P. 2002, ApJ, 564, 981
Proffitt, C. R., Brown, T. M., Mobasher, B., & Davies J. 2003, Absolute Flux Calibration of STIS MAMA Imaging Modes (Baltimore: STScI)
Rajagopal, M., & Romani, R. W. 1997, ApJ, 491, 296
Rajagopal, M., Romani, R. W., & Miller, M. C. 1997, ApJ, 479, 347
Romani, R. W. 1987, ApJ, 313, 718
Romani, R. W., Kargaltsev, O. Y., & Pavlov, G. G. 2005, ApJ, in press
Romani, R. W., & Yadigaroglu, I.-A. 1995, ApJ, 438, 314
Ruderman, M. 2003, preprint (astro-ph/0310777)
Seaton, M. J. 1979, MNRAS, 187, 73P
Serafimovich, N. I., Shibanov, Yu. A., Lundqvist, P., & Sollerman, J. 2004, A&A, 425, 1041
Shearer, A., et al. 1998, A&A, 335, L21
Shitov, Yu. P., & Pugachev, V. D. 1998, NewA, 3, 101
Sollerman, J., Lundqvist, P., Lindler, D., Chevalier, R. A., Fransson, C., Gull, T. R., Pun, C. S. J., & Sonneborn, G. 2000, ApJ, 537, 861
Strickman, M. S., et al. 1996, ApJ, 460, 735
Thompson, D. J., Fichtel, C. E., Hartman, R. C., Kniffen, D. A., & Lamb, R. C. 1977, ApJ, 213, 252
Trümper, J., Burwitz, V., Haberl, F., & Zavlin, V. E. 2004, Nucl. Phys. B Proc. Suppl., 132, 560
Turbiner, A. V., & López Vieyra, J. C. 2004, Mod. Phys. Lett. A, 19, 1919
Van Adelsberg, M., Lai, D., & Potekhin, A. Y. 2004, ApJ, submitted (astro-ph/0406001)
Wang, F. Y.-H., Ruderman, M., Halpern, J. P., & Zhu, T. 1998, ApJ, 498, 373
Yakovlev D. G., & Pethick C. J. 2004, ARA&A, 42, 169
Zavlin, V. E., & Pavlov, G. G. 2002, in Proc. 270 Heraeus Seminar on Neutron Stars, Pulsars, and Supernova Remnants, ed. W. Becker, H. Lesch, & J. Trümper (MPE Rep. 278; Garching: MPE), 263
———. 2004a, ApJ, 616, 452
———. 2004b, Mem. Soc. Astron. Italiana, 75, 458
Zavlin, V. E., Pavlov, G. G., & Sanwal, D. 2004, ApJ, 606, 444
Zhang, L., & Cheng, K. S. 2001, MNRAS, 320, 477